CONTINUUM GENERATION IN ULTRA HIGH NUMERICAL APERTURE FIBER WITH APPLICATION TO MULTIPHOTON MICROSCOPY

by

Nicholas Sayler

A thesis submitted to the Faculty and the Board of Trustees of the Colorado School of Mines in partial fulfillment of the requirements for the degree of Master of Science (Applied Physics).

Golden, Colorado

Date ________________________

Signed: ________________________
Nicholas Sayler

Signed: ________________________
Dr. Jeff Squier
Thesis Advisor

Golden, Colorado

Date ________________________

Signed: ________________________
Dr. Tom Furtak
Professor and Head
Department of Physics

ABSTRACT

Nonlinear microscopy benefits from broadband laser sources, enabling efficient excitation of an array of fluorophores, for example. This work demonstrates broadening of a narrow band input pulse (6 nm to 40 nm) centered at 1040 nm with excellent shot-to-shot stability. In a preliminary demonstration, multiphoton imaging with pulses from the fiber is performed. In particular second harmonic imaging of corn starch is performed.

TABLE OF CONTENTS

LIST OF FIGURES

LIST OF ABBREVIATIONS

Photonic Crystal Fiber	PCF
Supercontinuum	SC
Self-Phase Modulation	SPM
Second Harmonic Generation	SHG
Multiphoton Microscopy	MPM
Differential Multiphoton Laser Scanning Microscopy	dMPLSM
Multiphoton Absorption	MPA
Third Harmonic Generation	THG
Two Photon Excitation	TPE
Two Photon Fluorescence	TPF
Laser Scanning Microscopy	LSM
Single Photon Absorption	1PA
Multifocal Multiphoton Laser Scanning Microscopy	mfMPLSM
Polarizing Beam Splitter	PBS
Multiphoton Laser Scanning Microscopy	MPLSM
Ytterbium-doped Potassium Gadolinium Tungstate	Yb:KGW
One Photon Excitation	1PE
One Photon Excitation Fluorescence	1PEF
Group Velocity Dispersion	GVD
Zero Dispersion Wavelength	ZDW

Group Delay Dispersion . . . . GDD

Non-linear Schrodinger Equation . . . . NLSE

Optical Coherence Tomography . . . . OCT

Coherent Anti-Raman Spectroscopy . . . . CARS

Full Width at Half-Maximum . . . . FWHM

Cross-correlation Frequency Resolved Optical Gating . . . . XFROG

Relative Noise Intensity . . . . RIN

Two Photon Excitation Fluorescence . . . . TPEF

Numerical Aperture . . . . NA

Continuous Wave . . . . CW

Two Photon Absorption . . . . TPA

Signal to Background Noise Ratio . . . . SBR

Stimulated Raman Scattering . . . . SRS

Fast Fourier Transform . . . . FFT

Charge-Coupled Device . . . . CCD

Ultra High Numerical Aperture . . . . UHNA

Working Distance . . . . WD

Spherical Aberration . . . . SA

Photo-Multiplier Tube . . . . PMT

Field Programmable Gate Array . . . . FPGA

CHAPTER 1

INTRODUCTION

The development of photonic crystal fibers (PCFs) capable of generating super- continuum (SC) broadband light useful in the excitation of multiple fluorophores is discussed in this section. Multi- photon microscopy (MPM) is introduced in section 1.1, with an overview of the historical development as well as conceptual understanding. Section 1.2 extends this to a more complex system of differential multiphoton laser scanning microscopy (dMPLSM), showing the abilities of MPM in image acquisition. Section 1.3 discusses fluorophores and their use in biological imaging. Section 1.4 begins inquiry into the historical development of the use of PCFs, both in use and theory. The final portion of the introduction address the shot-to-shot stability and noise issues previously encountered when attempting to use PCFs for similar applications. As a remedy to these problems, we present the use of a ultra high numerical aperture (UHNA) optical fiber which can create a continuum capable of spanning a frequency range sufficient to excite common fluorophores in the 500-550 nm range through two photon excitation (TPE). The use of this UHNA fiber corrects the problem of shot-to-shot noise instabilities, leading to a more advantageous use in MPM.

1.1 Multiphoton Microscopy

Multi-photon microscopy (MPM) is a non-linear optical phenomena that is based on molecular excitation by multi-photon absorption (MPA). It was first used in microscopy to produce second harmonic generation (SHG) images of crystals by Hellwarth and Christiansen in 1974, and by Sheppard and Kompfner in 1978 [1] [2]. It is commonly used for second harmonic generation (SHG) or third harmonic generation (THG), in which two or three photons are destroyed, and one photon with a wavelength of one-half or one-third the original is created. Denk et. al. applied MPM to biological imaging for the first time in 1990 [3]. When being used for biological imaging, it commonly uses red-shifted excitation light in which two photons are absorbed to excite the fluorescent dyes, referred to as two photon excitation (TPE). The relaxation wavelength of the fluorophore, referred to as two photon fluorescence (TPF), is then red-shifted from the virtual transition of the SHG wavelength, by an amount called the Stokes parameter. In all instances of SHG, THG, and TPE, the intermediate state between the absorption of one photon and the absorption of the next is not a metastable state. Since there can be essentially no time delay between the arrival of the two photons, these phenomena refer to simultaneous absorption, as opposed to sequential absorption. Figure 1.1 shows the virtual transitions of SHG and THG, along with the real transition of TPF. The Stokes parameter in this case is

$$h\nu_{SHG} - h\nu_{TPF} \tag{1.1}$$

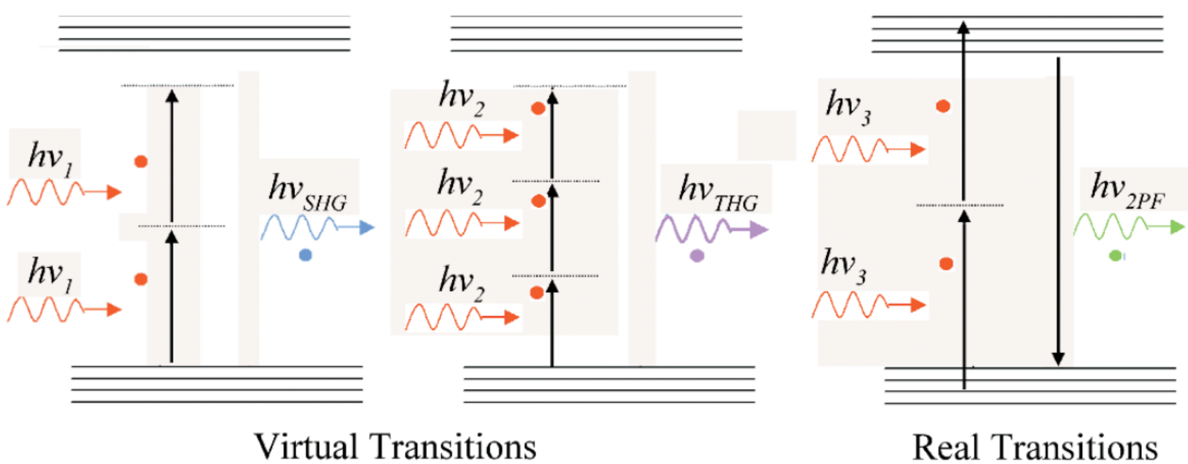

Figure 1.1: Energy state diagram. No energy is absorbed by the specimen for SHG and THG, resulting in the SHG frequency being twice that of the incoming frequency, and the THG frequency being three times that of the incoming frequency. For TPF, a fluorophore in the specimen absorbs two photons to raise it to an excited state. It then fluoresces to the ground state at a wavelength more than half of the incident wavelength.

With the development of laser scanning microscopy (LSM) in 1969 by Davidovits and Egger, the amount of time required to obtain an image from a sample was greatly reduced. Because excitation is dependent on a power of the intensity, the advantage over conventional fluorescence microscopy is that the fluorescence from out-of-focus elements is reduced without use of a confocal spatial filter. To optimize use for biological imaging, two conditions should be met: single photon absorption (1PA) should be minimized so that heating and photodamage is reduced, and peak intensity should be maximized, since the transition probability for TPA depends on the square of the intensity. Therefore, the optimal use for biological imaging at a given power is to use short, intense pulses with a small duty cycle. The development of mode-locked lasers that are capable of generating pulses shorter than a picosecond with high repetition rates have increased the usefulness of MPM techniques.

Despite the prediction of MPM in 1931 by Goeppert-Mayer, it took until the invention of the laser in 1960 for it to be experimentally confirmed [5] [6]. The first experimental observation of a two-photon excitation was in 1961 by Kaiser and Garrett, with the observation of three-photon excitation following soon after in 1964 by Singh and Bradley [7] [8]. Many spectroscopic studies soon followed to explore the different quantum-mechanical selection rules that apply to TPE [9] [10] [11] [12] [13]. They showed that for isolated atoms a transition allowed for 1PA would be strictly forbidden for TPA and vice versa. However, due to their reduced symmetry and the effect of molecular vibrations, strict parity selection rules do not usually hold for complex dye molecules [14].

In this experiment, SHG of corn starch is exploited. The starch granule is commonly used because of its ability to produce a strong SHG signal due to its lack of centro-symmetry. This lack of symmetry is caused by its orderly nanolayers of amylopectin side-chain clusters within the crystalline lamellae forming a biophotonic structure. These amylopectin side chains are interleaved with more amorphous lamellae consisting of the amylopectin branching regions. As seen in Figure 1.2, these crystalline lamellae organize into spherical blocklets and large concentric growth rings, and exhibit highly birefringent structure [15]. The large SHG activity may also be seen as a collection of 3D photonic bandgap crystals, capable of producing SHG by meeting the non-collinear phase matching condition. This 3D nonlinear photonic bandgap crystal behavior arises from larger structures of crystalline hard shells and semi-crystalline soft shells with spatially-modulated nonlinear properties [16].

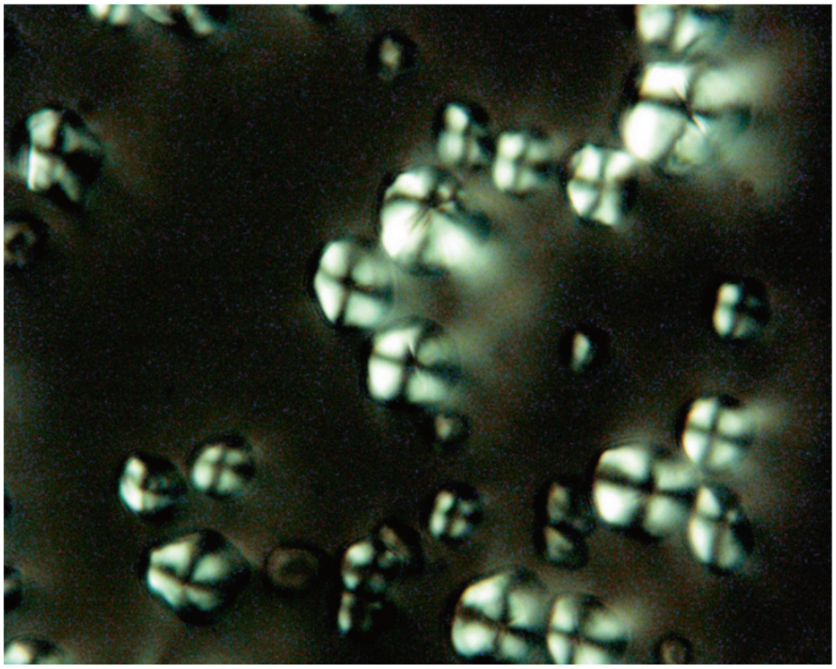

Figure 1.2: Polarization microscopy of corn starch granules. The image was taken with an oblique-illuminated microscope equipped with cross-polarizer. Dimensions are approximately 1 μ m x 1 μ m. Image taken from [17].

1.2 Differential Multiphoton Laser Scanning Microscopy (dMPLSM)

Laser scanning microscopy was developed in 1978 by Cremer and Cremer to allow for greater depth of focus of an image by using point-to-point scanning [94]. The additional use of multi-photon microscopy by Denk et. al. in 1990 led to the development of multifocal multiphoton laser scanning microscopy (mfMPLSM) by Brewersdorf in 1998 [3] [95]. This technique of separating a single excitation focus into several foci allows for high speed image acquisition because the area each focus must scan is decreased. However, a large restriction on mfMPLSM is the requirement of imaging detectors to map the nonlinear signal generated by each focus [96]. This usually results in scattering imaging points interfering with each other, leading to a reduction in resolution.

A solution to this was proposed by Field et. al. to use a PMT to measure the nonlinear signal generated by each focus inside the sample [93]. This differential multiphoton laser scanning microscopy (dMPLSM) setup required optical multiplexing and electronic demultiplexing to allow for greater resolution imaging when compared to mfMPLSM, as shown in Figure 1.3.

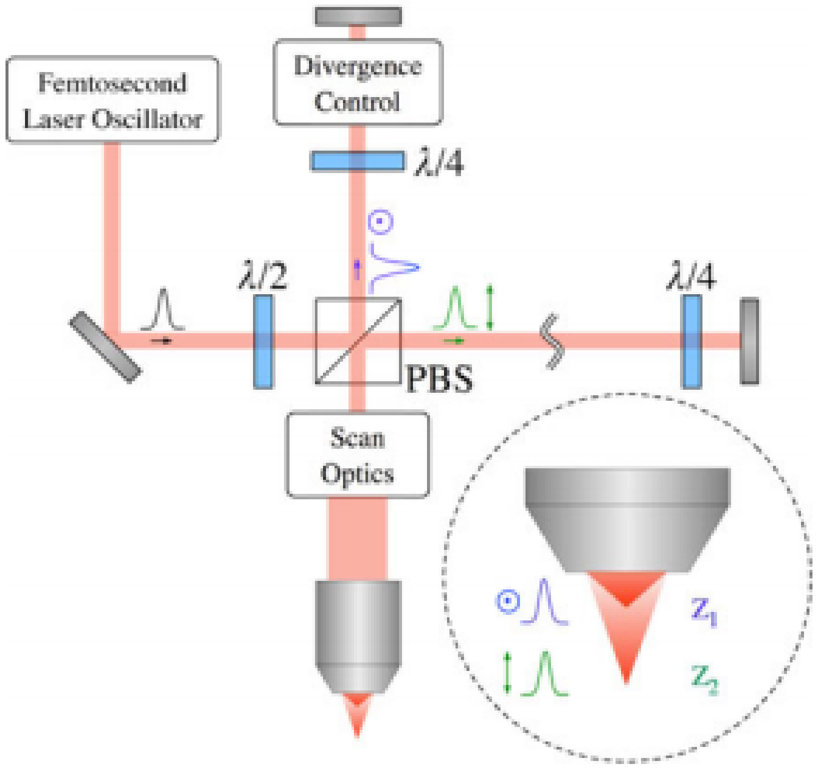

Figure 1.3: Optical demultiplexing used for the dMPLSM system. Two collinear beams generate orthogonally polarized foci in the sample plane, while optical delay is introduced by path length modulation with use of a polarizing beam splitter (PBS) for interlacing of pulse trains. Image taken from [93].

Each beam is spatially separated, allowing for multiple modalities to be generated with each shot. The result is a set of simultaneous images that highlight the differences resulting from varied excitation parameters. In this process, two planes were imaged simultaneously. This could be expanded to decrease the scan time, as in MPLSM, simultaneous imaging of up to six planes has been demonstrated [97] [98]. To increase the usefulness of this technique, multiple fluorophores can be used to tag different features of interest within the cell. Field et. al. attempted use of a PCF to generate the bandwidth required to excite these multiple fluorophores. In order to exploit the advantages of dMPLSM, we increase the shot-to-shot stability by use of a ultra high numerical aperture (UHNA) optical fiber, compared to the experiment by Field et. al. [93].

1.3 Fluorescent Imaging

A fluorophore is a chemical compound that absorbs light of a certain wavelength, and re-emits light of a longer wavelength, with the difference between wavelengths being referred to as the Stokes shift. With the exception of the potential application of quantum dots as fluorophores, current improvement in fluorophores is sparse [18] [19] [20]. Absorption spectra for various fluorophores for wavelengths between 300 and 700 nanometers are given in Figure 1.4. Multi-photon microscopy (MPM) has not commonly been used for biological imaging below 300 nm because of the potential for photodamage at high energies [21] [22] [23] [24] [25] [26].

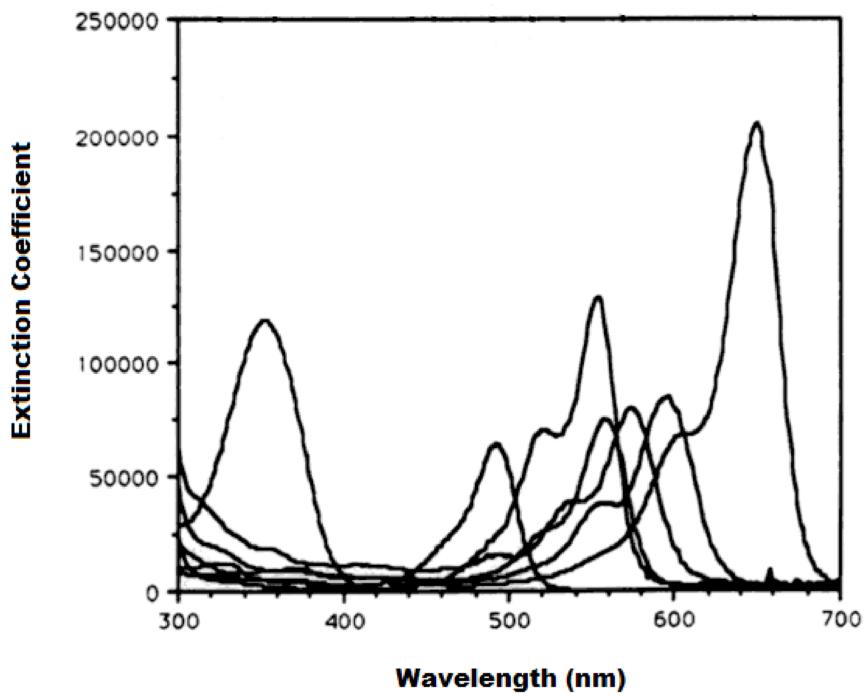

Figure 1.4: Absorption spectra from left to right of Hoechst 33342+DNA, and fluorescein, CY3, TRITC, lissamine rhodamine B, Texas Red, and CY5 conjugated to antibodies. Extinction coefficients are given on a per-dye basis. Image taken from [17].

Ytterbium-doped potassium gadolinium tungstate (Yb:KGW) lases at a primary wavelength of 1040 nm, which takes advantage of the dip in the absorption spectrum of water at that wavelength, in order to minimize scattering in biological samples [26]. Making this a supercontinuum broadband laser source from non-linear optical processes, it would have the ability to excite multiple fluorophores simultaneously with TPE, allowing for marking of different points of interest within biological samples according to fluorophore. This imaging could allow differentiation of molecules within the sample as well as depth imaging with rejection of out of focus elements.

For fluorophores with a known single-photon spectrum, some TPE usually occurs at twice the frequency of the frequency at which one photon excitation (1PE) occurs, that is to say, they both lead to the same fluorescence wavelength [27]. States that are inaccessible to 1PE because of their slightly higher energy and lack of wave-function overlap with the ground state can sometimes be reached with TPE through intermediate virtual states that overlap with both the initial and the final state [9] [28] [29]. This results in two photon spectra that are generally broader than single-photon spectra. In addition, if any additional features appear on the TPEF spectrum, it is always on the short wavelength side of the spectrum, in comparison to the one photon excitation fluorescence (1PEF) spectrum. This is because of the cutoff wavelength required to excite the fluorophore. Since the two-photon excitation is dependent on the two-photon cross-section quadratically, strongly absorbing single-photon fluorophores are often very strongly absorbing two-photon fluorophers, and weakly absorbing single-photon fluorophores tend to be very weakly absorbing two-photon fluorophores.

1.4 History of the use of Photonic Crystal Fibers (PCFs) used for this application

Photonic crystal fibers (PCFs) have been historically used to increase the frequency spectra due to their large bandwidth spread. In this section, we look at the detail of these fibers.

Conventional optical fibers operate through total internal reflection, in which the core and the surrounding air hole region (cladding) have differing indices of refraction. Guidance occurs at the boundary between the two concentric glass cylinders, at which the difference in refractive index is on the order of 0.1%. Characteristics of this type of propagation have been closely studied [30]. PCFs are different from conventional optical fibers in that they are composed of regularly repeating alternating regions of high and low dielectric constant that affect the propagation of electromagnetic waves in the same way as the periodic potential in a semiconductor crystal affects the electron motion by defining allowed and forbidden electronic energy bands. This concept of guidance was first suggested by Kaiser and Astle in 1974 [31]. The term photonic crystal fiber was coined by Russell in an idea to confine and guide white light through optical fiber using a periodic array of microscopy air holes that run along the entire fiber length [32]. This was first realized by Knight et. al. in 1996, which then lead to a large amount of interest and experimentation in PCFs [33].

There are two types of PCFs: hollow core PCFs and solid core PCFs. Hollow core PCFs have shown potential for use in lossless and distortion-free transmission, particle trapping, optical sensing, and various other nonlinear optical applications [34] [35] [36] [37]. However, hollow core PCFs do not create very broad spectral bandwidth, and hence supercontinuum. Supercontinuum (SC) generation is a process by which essentially monochromatic laser light is converted to a very broad spectral bandwidth, while generally maintaining high spatial coherence. In dispersive PCFs, dispersion plays a role in expanding the spectrum on all pulses. In nanosecond and picosecond pulses in PCFs, SC generation is mainly achieved by Raman scattering and four-wave mixing. In femtosecond pulses, SC generation is mainly achieved through self-phase modulation (SPM). We will then focus on solid core PCFs which are used in SC generation experiments, and in this experiment.

A solid core PCF consists of a uniform refractive index material in which a microstructure lattice of air holes is embedded that runs along the fiber length, as shown in Figure 1.5. The removal of an air hole in the center introduces a defect associated with a locally elevated refractive index, and guided wave propagation within this elevated index region occurs through total internal reflection. If the microstructure of the PCF exhibits perfect rotational symmetry, the SC generation has no sensitivity to input polarization. However, if any asymmetries are introduced in the microstructure fabrication, the fiber can show residual birefringence and polarization-maintaining behavior [59]. This is expanded on in the birefringence section.

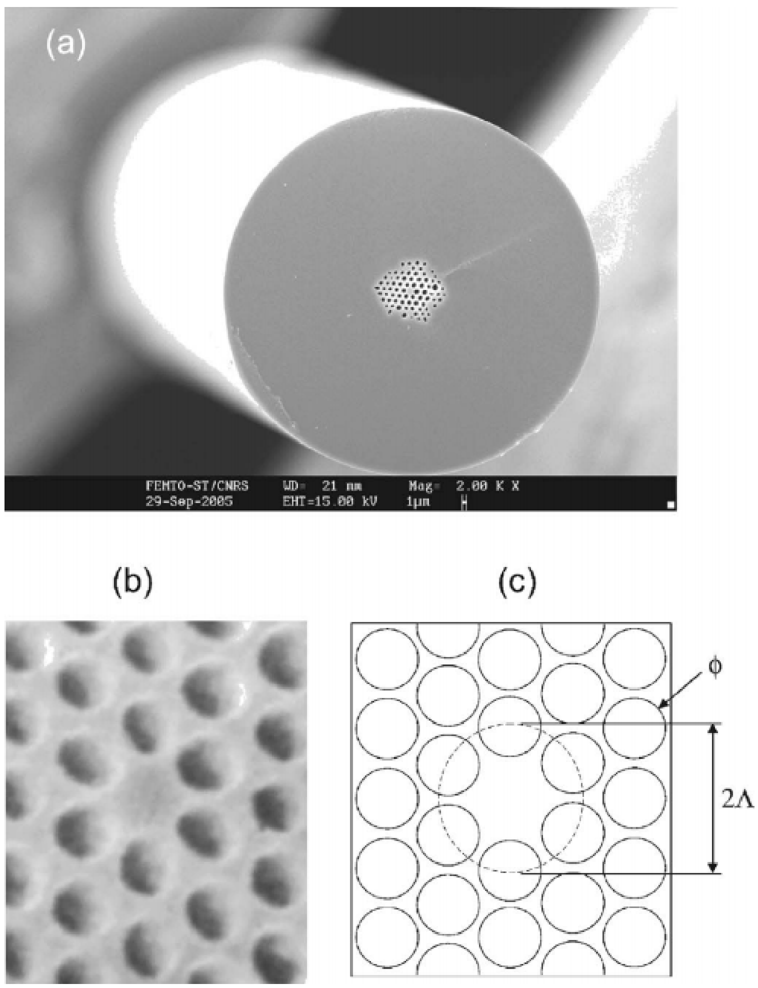

Figure 1.5: Photonic crystal fiber structure. (a) Electron micrograph of the PCF used in SC generation. (b) Detail of central microstructure and (c) ideal hexagonal structure. Image taken from [41].

Chromatic dispersion of the fundamental mode determines the phase velocity of the various wavelengths within the pulse. The phase velocity is defined as

$$v_p = \omega/\beta(\omega) \tag{1.2}$$

where ω is angular frequency and β is the wavenumber. This can be expanded in a Taylor series about the central pulse frequency ω_0 as

$$\beta(\omega) = \beta(\omega_0) + \beta_1(\omega_0)\Omega + (1/2)\beta_2(\omega_0)\Omega^2 + (1/6)\beta_3(\omega_0)\Omega^3 + ... \tag{1.3}$$

where $\Omega = \omega - \omega_0$ and

$$\beta_k(\omega_0) = \frac{d^k\beta}{d\omega^k}|_{\omega_0} \tag{1.4}$$

The physical interpretation of the first term is simply the refractive index of the medium of propagation, while the second term is the inverse of the group velocity of the pulse. The third term, β_2, is the group delay dispersion (GDD), which is commonly referred to through the GDD parameter given as:

$$D = -\frac{2\pi c}{\lambda^2}\beta_2 \tag{1.5}$$

Solid core PCFs have a region of solid glass surrounded by an array of air holes running along its length, which provides for a difference in the index of refraction which is enough to cause guidance through modified total internal reflection [38]. Because of the ability given to determine the hole diameter and periodicity of the structure, properties of the PCF can be changed in order to accommodate certain uses. Most importantly, the zero dispersion wavelength (ZDW) can be dialed to a desired value in order to create a symmetric spectrum from the fiber [39].

The ZDW is the wavelength at which the group delay dispersion (GDD) and hence the GVD is zero. The intrinsic ZDW of silica used in conventional optical fiber is 1.3 μm. The manipulation of the ZDW, with the added effects of SPM allow for great manipulation over the outgoing spectrum. The ZDW can be tuned by adjusting the core diameter, controlling the amount of guiding contribution to the phase. It was noted by Broderick et. al. in 1999 that changing the hole diameter also reduces the effective area of the propagating mode in this type of fiber, leading to enhanced Kerr nonlinearity and hence greater bandwidth expansion by SPM [40]. This was demonstrated by Ranka et. al. in 2000 by generating a SC spanning over an octave from 400 to 1500 nm with a ZDW around 765-775 nm, and soon after by Wadsworth et. al. with a ZDW at 850 nm [41] [42]. An advantage over bulk SC generation was that the wavelength components did not create filamentation, and retained a uniform spatial profile through propagation.

The mechanisms of nanosecond and picosecond SC generation through PCF was soon discovered with the works of Provino et. al. and Coen et. al. in 2001 [43] [44]. Provino et. al. used 0.8 ns pulse duration for SC generation, based on the parametric gain calculations of cascaded Raman scattering and four-wave mixing. Coen et. al. showed the first use of a generalized non-linear Schrodinger equation (NLSE) including higher-order dispersion and Raman scattering to model the SC generation using pulses 60 ps in duration.

For femtosecond pulses, using a similar approach to Coen et. al., Liu et. al. used an extended NLSE limited to cubic dispersion terms to model simulations of SC generation in good agreement with experiment [45]. Washburn et. al. also created a femtosecond model focusing on Raman solitons generated during the SC generation process, which also agreed well with experiment [46]. Husakou and Herrmann were the first to create a numerical model of femtosecond SC generation in PCFs that included soliton fission in 2001 [47]. Their calculations failed to incorporate Raman scattering and did not agree well with experiment [48].

Further simulation and experiment in the following years expanded in further detail the interplay of mechanics involved, but the basic groundwork was in place by 2002. The consensus was that soliton fission and Raman self-frequency shift was responsible for the long-wavelength components of the SC, while the short-wavelength components were accounted for by dispersive wave generation.

The utilization of SC generation from PCFs for imaging was first exploited by Hartl et. al. in 2001 for use in optical coherence tomography (OCT) [79]. The broad spectrum generated from the PCF allows ultrahigh resolution in OCT, leading to further experiments [80] [81] [82] [83]. In addition, coherent anti-Stokes Raman scattering spectroscopy (CARS) has been a useful application for SC generation, where Andresen et. al., demonstrated a spectral resolution improvement of over one order of magnitude better than a transform-limited spectrally compressed pulse [84]. Photonic crystal fiber (PCF) SC generation for CARS has been used for further optical imaging [85] [86] [87].

With respect to fluorescent microscopy, McConnell first used PCF SC in confocal fluorescent microscopy in 2004 to be able to excite multiple fluorophore labels for imaging [88]. Further experiments have expanded use to MPM, and demonstrated the usefulness in PCF SC generation for application in MPLSM, and dMPLSM [89] [90] [91] [92]. Using the same laser oscillator used in this experiment, Field et. al. were able to generate SHG from 380 nm to 600 nm in corn starch molecules [93].

1.4.1 Modality

A certain type of PCFs have been shown to have the ability to propagate endlessly in a single mode, suppressing all higher-order mode behavior [38]. These PCFs have relatively small air-fill fraction and large core areas when compared with other solid core PCFs. This single mode PCF is not used in SC generation because the small air-fill fraction leads to weak confinement of the mode and nonlinear effects are reduced. Therefore, the PCFs used in SC generation have high air-fill fraction and smaller core areas compared to single mode PCFs. As a result, SC PCFs can exhibit multimode behavior, although to generate higher modes in high air-fill fraction solid core fiber requires high power pumping conditions [58]. The reason SC PCFs require high pumping energy to show multimode behavior is that there is a strong wave-vector mismatch between the fundamental and higher-order modes in the fiber.

1.4.2 Birefringence

Imperfections in the rotational symmetry of the fabrication of PCFs results in birefringence and polarization-maintaining behavior. Early construction of PCFs aimed at avoiding imperfections in the core of the microstructure, but after understanding their origin, some experiments have aimed at inducing birefringence in PCFs [60] [61].

In order to maximize the SC generation, the seed beam should be input along the principal polarization axis. This allows for the largest nonlinear index of refraction to affect the propagation of the beam. Supercontinuum (SC) generation through birefringent fiber exhibits polarization-maintaining behavior, where all frequency components of the output have the same polarization state as the pump. The fast and slow eigen-axes of the PCF act linearly independent of each other, with each SC spectra able to be obtained in terms of soliton and dispersive-wave dynamics, and different dispersion characteristics for each axis. It was shown by Lehtonen et. al. that the output state halfway between the two eigen-axes results from the linear superposition of the SC obtained independently on the two axes with half of the total input power on each [62]. The walkoff distance induced between the frequency components of each eigen-axis is small due within the short distance of propagation through the fiber leading to the linear independence of the axes [63].

1.5 The problem with these fibers for use with long pulse lasers like Yb:KGW

Of significant interest to this research is the evolution of the investigation of the SC intensity and phase stability properties. In 2000, it was first noticed in frequency metrology experiments where optical clockworks were interfered with by broadband noise at radio frequencies, this instability was further investigated and observed to be beyond the frequency roll-off of any laser technical noise [49] [50] [51]. In 2002, Gui et. al. demonstrated the origin of this noise is large shot-to-shot fluctuations of the SC generation [52]. The results from this numerical calculation of SC generation from a 800 nm seed pulse in PCF a FWHM $\Delta \tau = 30$ fs at 10 kW peak power show the shot-to-shot instabilities common in spectral and temporal intensity, as shown in Figure 1.6 [52]. Figure 1.7 shows the experimental shot-to-shot instabilities observed in cross-correlation frequency resolved optical gating (XFROG) measurements [52]. It was shown by Dudley and Coen, and by Gaeta that these spectral and temporal structures showed high sensitivity to input pulse noise [53] [54]. By comparing simulations of decoherence with and without Raman gain, they showed that the cause of coherence degradation is primarily due to input shot noise and not spontaneous Raman scattering. In an average over many shots, this shot-to-shot variation could wash out the spectral fine structure and degrade spectral coherence.

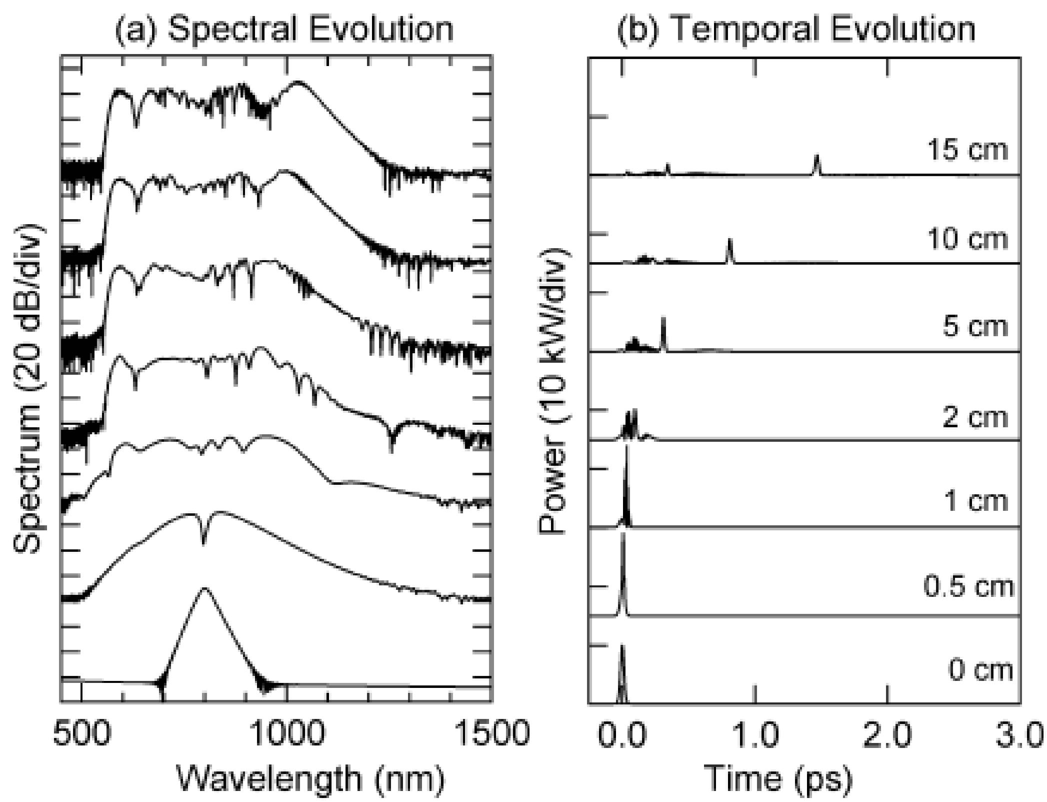

Figure 1.6: (a) Spectral and (b) temporal SC evolution of injected 10 kW peak power 30 fs input pulse at 800 nm in PCF. Image taken from [52].

In 2003, Corwin et. al. embarked on a detailed experimental and numerical study into the SC intensity noise characteristics [64]. They found that the median relative intensity noise (RIN) increased with input pulse chirp and duration and attained its minimum value

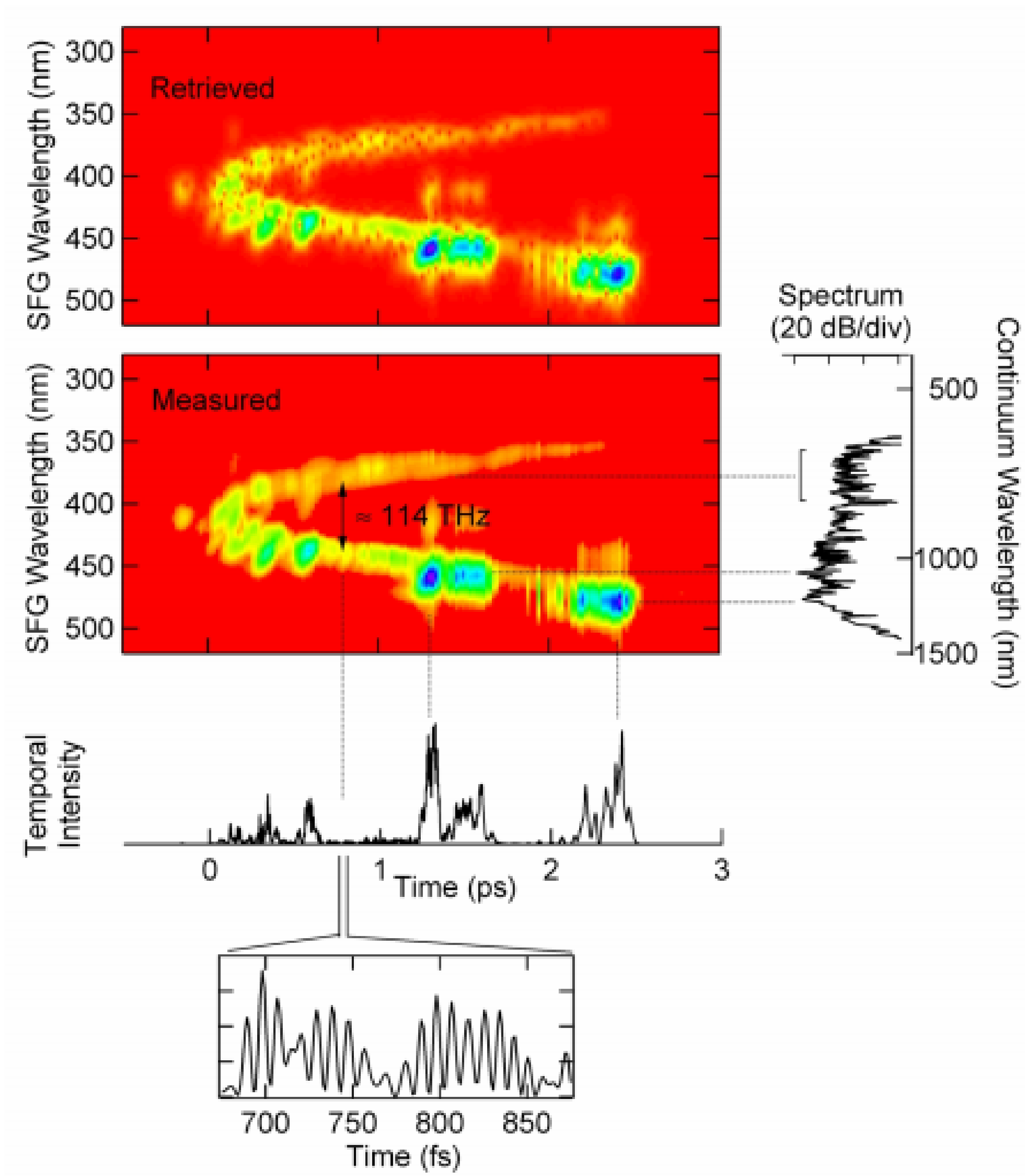

Figure 1.7: Measured and retrieved XFROG traces with the structure of the measured trace correlated with the retrieved intensity and spectrum. Image taken from [52].

when the input pulses were transform-limited around 22 fs in duration. This was confirmed by later experiments as well [65] [66]. In order to better observe the dependence on intensity modulation input to a PCF for SC generation, and acousto-optic modulator was used by Haverkamp and Telle [67]. They were able to extract an effective complex intensity modulation transfer function by characterizing the SC output as a function of intensity and wavelength.

To find the mutual degree of coherence, Gui et. al. input pulses into two separate PCFs and observed the wave pattern from interferometric measurement [68]. The input pulses were at 800 nm, and the ZDW of the PCF was at 760 nm. The average coherence integrated over the SC spectrum was relatively low, attributed to technical noise and different pulse energies for each segment. A similar experiment was carried out by Lu and Knox in 2004, using input wavelengths over the range of 780-920 nm through a PCF with a ZDW of 820 nm [69]. Clear degradation in SC coherence was measured as the pump wavelength was tuned into different GVD regimes. Later experiments, along with numerical simulations, led to characterization of coherence, further explained in the theory section [70] [71]. Coherent SC generation can be realized by pumping the PCF in the normal GVD regime, but the downside to the coherent SC is that the spectral width is much smaller due to rapid initial temporal spreading of the pump pulses.

Shot-to-shot stability and coherence properties also played a role in possible ways to generate ultra-short pulses on the order of individual femtosecond pulse widths, which gained interest through compression of these SC, because of the large bandwidths. This was first suggested by Husakou and Herrmann in 2001, but early experiments were limited to pulse widths of only 20-25 fs [47] [72] [73] [74]. The reason for this was pointed out by Dudley and Coen in showing that the generation of a SC that was compressible was equivalent to the generation of one that was coherent [75]. In other words, the amount of compression was limited by the coherence of the SC [76]. To compensate for the shot-to-shot instability, use of adaptive phase compensation through a spatial light modulator-based pulse shaper technology was incorporated by Schenkel et. al. in 2004 to reach pulse lengths of 5.5 fs [77]. This pulse width was then reduced further to 4.8 fs by Adachi et. al. in 2005 by carrying out filtering and selective compression only over the fraction of the SC spectral bandwidth with the highest coherence [78].

The problems of modulation instability from shot-to-shot noise are solved in this experiment by using a ultra high numerical aperture (UHNA) optical fiber for generation of the continuum. This allows use of one laser to generate the wavelengths necessary to excite multiple fluorophores within a sample, reducing the complexity and difficulty of having to use multiple lasers through a microscope on one sample. In addition, by separating the beam through different filters and lengths, multiple pieces of data can be obtained through one shot of the laser, reducing scan time and allowing for more information to be obtained.

CHAPTER 2

THEORY

The theory section begins with defining the advantage of MPM in imaging, and then moves to the theoretical description of the noise issues in section 2.2. Numerical calculations begin in section 2.3 with simulations of self-phase modulation (SPM) without dispersion, and section 2.4 covers simulations of dispersion without SPM. We then finish the theory section with numerically combining SPM and dispersion in section 2.5.

2.1 Two Photon Excitation Fluorescence(TPEF)

The probability p_a that a fluorophore at the center of the focus absorbs a photon pair during a single pulse is given by:

$$p_a = \delta < P >^2 F_p^{-1} (\frac{\pi NA^2}{2\pi \hbar c \lambda})^2 \xi \tag{2.1}$$

where δ is the two-photon cross-section, $< P >$ is the average power, F_p is the repetition frequency, λ is the wavelength, c is the speed of light in a vacuum, $\hbar$ is the Planck quantum of action, ξ is the advantage factor, and NA is the numerical aperture [3]. This is only an appropriate approximation for values of p_a that are much less than unity. This is because the molecule does not have enough time to fluoresce and re-absorb within the same femtosecond pulse. When the probability to absorb a photon pair approaches one, saturation effects begin to occur. Because TPA is dependent on the power squared, while undesirable 1PA effects are dependent on the average power, the two-photon advantage factor is defined as the average square of the power over the average power squared. This is calculated as:

$$\xi = \frac{< P^2 >}{< P >^2} = \frac{(t_1 - t_2)\int_{t_1}^{t_2} P^2(t)dt}{(\int_{t_1}^{t_2} P(t)dt)^2} \tag{2.2}$$

For a Gaussian pulse with a width τ_p (time between the half-power points) the advantage factor is $\xi \approx (F_p\ \tau_p)$-10.664, and for a hyperbolic-secant shaped pulse, the advantage factor is $\xi \approx (F_p\ \tau_p)$-10.558 [17]. This advantage for n-photon excitation is proportional to the inverse excitation duty cycle to the n^{-1} power. Therefore, a 100 MHz repetition rate using 100 fs pulses leads to a 100,000-fold improvement over CW (continuous wave) TPA.

Assuming a uniform fluorophore and taking into account that the beam cross-section at the surface varies as z^2, we find that the signal-to-background ratio of TPEF is given by:

$$SBR = \frac{2\pi(NA)^2}{n}\frac{z^2}{\lambda l_s}e^{-\frac{2z}{l_s}} \tag{2.3}$$

where NA is the numerical aperture, n is the index of refraction, and λ is the wavelength [55]. This high localization of excitation leads to high depth resolution and rejection of out-of-focus elements, as the electric field at out of focus points is dependent on the NA. An example of TPEF and intensity is given in Figure 2.1.

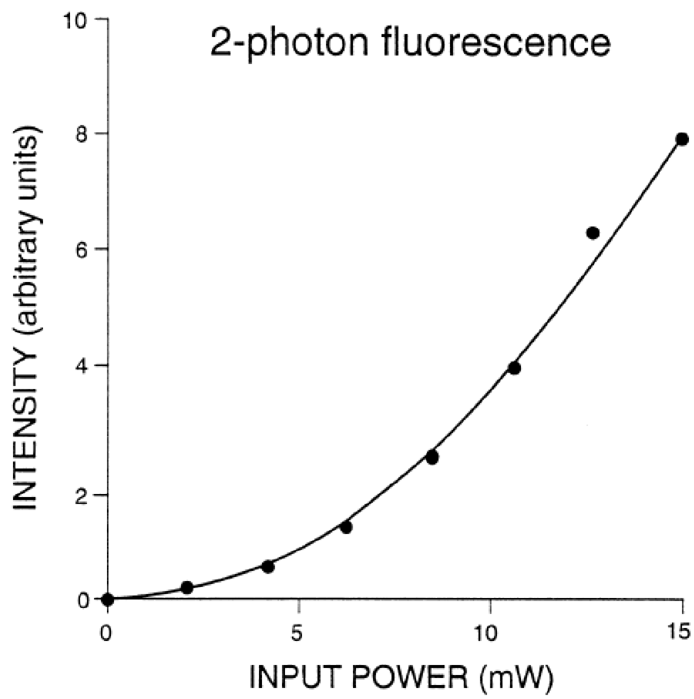

Figure 2.1: Fluorescence intensity generated in a uniformly labeled fluorescent block specimen as a function of laser power input into the microscope objective. The filled circles are the measured points and the continuous line is a second-order polynomial fit through the data, illustrating the quadratic dependence expected in two-photon fluorescence excitation. Image taken from [56].

2.2 Conventional Characterization of Decoherence

It was shown in Nakazawa et. al. in 1998 that modulation instability in conventional fibers can amplify low level noise at the input which can result in large fluctuation in the amplitude and duration of subsequently generated fundamental solitons [99]. In PCFs, spontaneous emission is not usually the source of the noise seed, instead the pump laser shot noise causes such fluctuations. These fluctuations are then converted into wavelength fluctuations through the solition self-frequency shift, which in turn leads to significant temporal jitter through the effect of chromatic dispersion. Noise effects are exaggerated in PCFs compared to conventional fibers because of the high nonlinearity induced. Kubota et. al showed that the coherence of the pump beam can be maintained by using a dispersion-decreasing fiber and the adiabatic soliton compression of N>1 fundamental solitons, or by pumping at a wavelength significantly below the ZDW, so that modulation instability does not occur [100]. Another solution to avoiding SC decoherence was proposed by Nowak et. al. to shorten the fiber length so that the pump pulses only propagate over a fraction of a soliton period in such a way that the spectral broadening process is interrupted when the soliton has maximum bandwidth before fission can happen [101]. This distance is referred to as the fission distance $L_{fiss} \sim L_D/\mathrm{N}$, where L_D is the length of the fiber, and N is the order of the soliton.

Because modulation instability scales with the length of the pulse, coherence degradation is larger with longer pulse lengths. In addition, at constant peak power, high-order solitons of shorter duration reach their fission distance faster resulting in less spatial dechoerence. The spectral extent of shorter pulses overlaps with the frequencies of maximum modulation instability gain before significant amplification of noise background has occurred, leading to more deterministic behavior. These results are shown in Figure 2.2.

The emergence of modulation instability seeded by noise is only an appreciable effect in the case that soliton fission does not occur first. Therefore, a dependence on wavelength can also be found since the decreased value of dispersion at shorter wavelengths results in

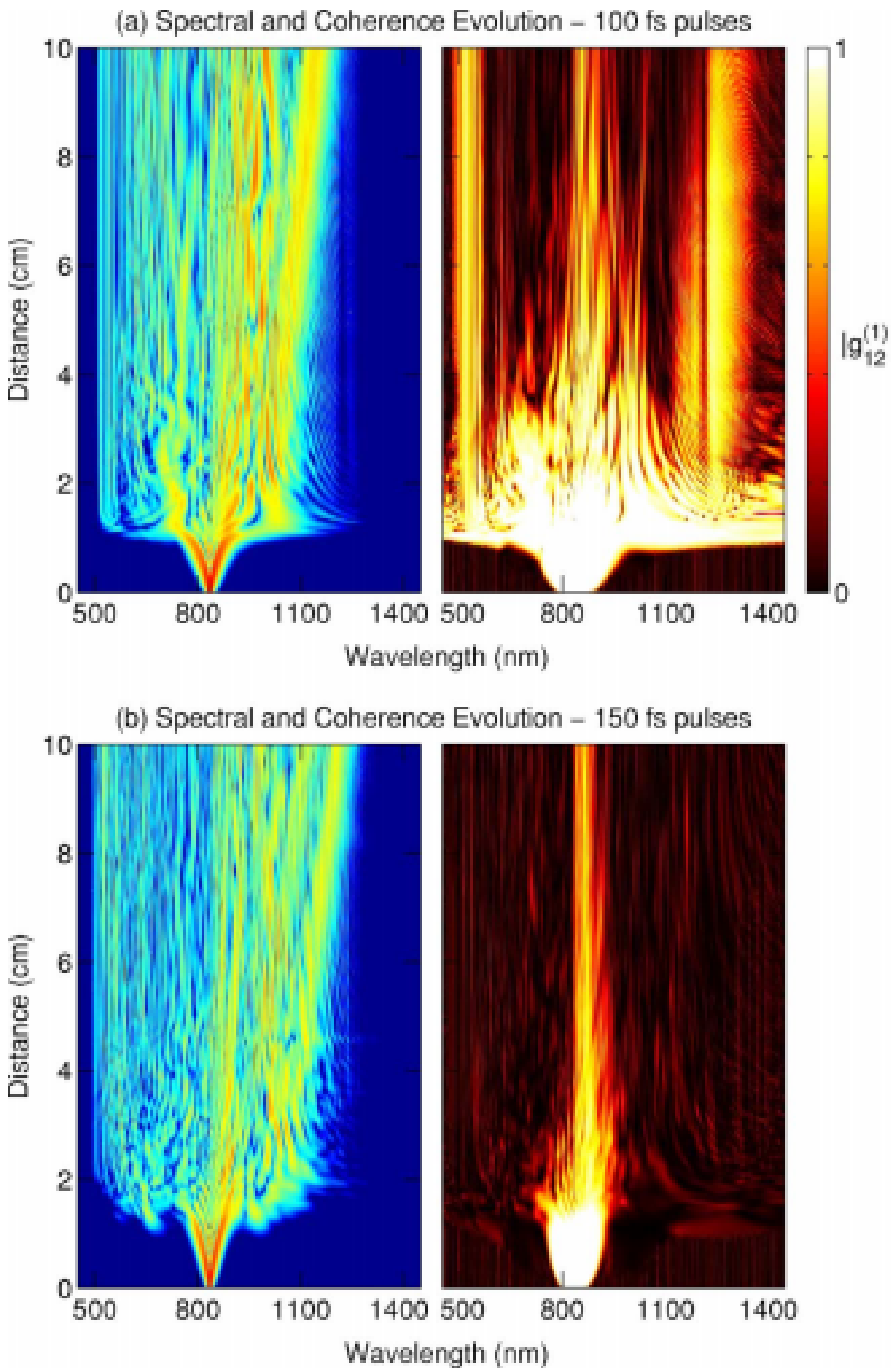

Figure 2.2: Evolution along the fiber length of the spectrum of one particular simulation (left) and of the corresponding degree of coherence (right) for supercontinuum generation obtained with 10 kW peak power pulses of (a) 100 and (b) 150 fs duration at a 835 nm pump wavelength. Image taken from [53].

an increase in the characteristic fission length, suppressing the amplification of modulation instability. The gain length parameter for modulation instability is proportional to nonlinear length only, and therefore does not change significantly with frequency [102]. The wavelength dependence of SC generation coherence characteristics from PCF is shown in Figure 2.3.

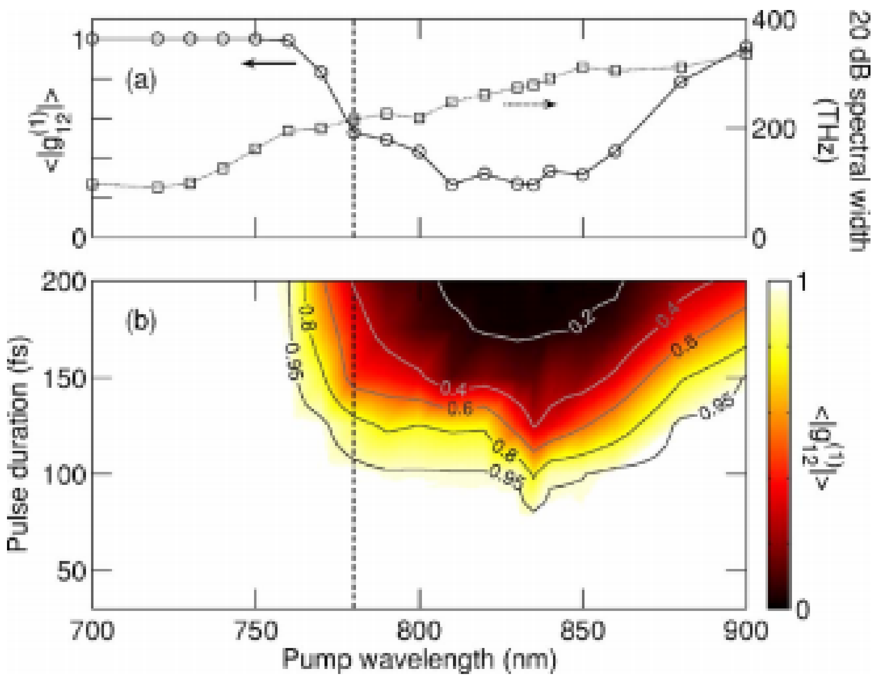

Figure 2.3: Wavelength dependence of coherence characteristics. (a) Dependence of the average coherence on pump wavelength (left axis) for SC obtained with 150 fs pulses of 4 kW peak power for 10 cm of PCF. Right axis shows the corresponding -20 dB SC spectral width. (b) Average coherence shown in a density plot representation as a function of both pump wavelength and pump pulse duration for a fixed peak power of 4 kW. The dashed line indicates the position of the ZDW. Image taken from [53].

2.3 Self-phase Modulation (SPM)

Self-phase modulation is a nonlinear optical phenomenon in which a laser beam propagating in a medium interacts with the medium to induce a phase modulation on the beam. The effect of SPM on a variety of experiments was quickly discovered after the discovery of the laser [103] [104] [105] [106] [107] [108] [109]. Due to the nonlinearity of the medium, the intensity of the beam creates a field strong enough to cause a change in the index of refraction of the medium. The reaction of the medium then induces a phase change on the incoming beam, resulting in SPM. Because the transverse intensity is not uniform, the wave front will be diffracted due to various degrees of SPM across the transverse face of the beam. This apparent self-diffraction from the spatial SPM gives rise to the nonlinear optical phenomena of self-focusing and self-defocusing [110] [111]. In pulsed lasers, the change in the temporal intensity leads to a SPM in time. Because the time derivative of the phase of a wave is the angular frequency of the wave, SPM can also be seen as a frequency modulation causing spectral broadening [105] [108] [112]. In order to maximize temporal SPM, we should choose a pulsed laser with a dynamic temporal profile. For a dynamic temporal profile, we look for a short laser pulse with high peak power, as this causes the greatest SPM.

Simple application of SPM considering only the lower-order effect was formulated early by on in parallel by Shimizu and Gustafson et. al. [108, 112] [108] [112]. Self-phase modulation (SPM) theory including higher-order contributions is not very theoretically complex, as long as dispersive effects of the optical material can be neglected, as shown in the mid-1980s [113] [114] [115]. Including dispersion greatly complicates things, and numerical solutions are generally applied.

2.3.1 Physical causes of SPM

A perturbative expansion in terms of the applied field is presented here as the nonlocal response is neglected. The induced polarization in a medium can be expressed as [116]:

$$\mathbf{P}(t) = \mathbf{P}^{(1)}(t) + \mathbf{P}^{(2)}(t) + \mathbf{P}^{(3)}(t) + ... \tag{2.4}$$

$$\mathbf{P}^{(1)}(t) = \int \chi^{(1)}(t-t')\mathbf{E}(t')dt' \tag{2.5}$$

$$= \int \chi^{(1)}(\omega)\mathbf{E}(\omega)e^{-i\omega t}d\omega \tag{2.6}$$

$$\mathbf{P}^{(n)}(t) = \int \chi^{(n)}(t-t_1, ..., t-t_n) : \mathbf{E}(t_1)...\mathbf{E}(t_n)dt_1...dt_n \tag{2.7}$$

$$= \int \chi^{(n)}(\omega = \omega_1 + \omega_2 + ... + \omega_n) : \mathbf{E}(\omega_1)...\mathbf{E}(\omega_n)d\omega_1...d\omega_n \tag{2.8}$$

where the applied field is

$$\mathbf{E}(t) = \int \mathbf{E}(\omega) e^{-i\omega t} d\omega \tag{2.9}$$

with

$$\mathbf{E}(\omega) \propto exp(-i\omega t) \tag{2.10}$$

and the n-th order susceptibility is

$$\chi^{(n)}(t - t_1, ..., t - t_n) = \int \chi^{(n)}(\omega = \omega_1 + ... + \omega_n) exp[i\omega_1(t - t_1) \tag{2.11}$$

$$+ ... + i\omega_n(t - t_n)] d\omega_1 ... d\omega_n \tag{2.12}$$

For a set of monochromatic applied fields we have

$$\mathbf{P}^{(n)} = \chi^{(n)}(\omega = \omega_1 + ... + \omega_n) : \mathbf{E}(\omega_1)...E(\omega_n) \tag{2.13}$$

For an instantaneous response corresponding to a dispersionless medium,

$$\mathbf{P}^{(n)} = \chi^{(n)} : [E(t)]^n \tag{2.14}$$

It is the third-order nonlinearity that gives rise to the change in refractive index, in which we only consider the self-induced refractive index change. Assuming a pulsed quasi-monochromatic field,

$$\mathbf{E}_\omega(t) = \mathcal{E}(t) exp(-i\omega t) \tag{2.15}$$

the third-order nonlinear polarization in a medium takes the form

$$\mathbf{P}^{(3)}_\omega(t) = \int \Delta\chi(t - t')\mathbf{E}_\omega(t')dt' \tag{2.16}$$

with

$$\Delta\chi(t - t') = \int \chi^{(3)}(t - t', t - t'', t - t''') : \mathbf{E}_\omega(t'')\mathbf{E}{*}_\omega(t'')dt''dt''' \tag{2.17}$$

If the optical field is sufficiently far from resonances that the traverse excitations are all virtual and can be considered as instantaneous,

$$\mathbf{P}^{(3)}_\omega(t) = \Delta\chi(t)\mathbf{E}_\omega(t) \tag{2.18}$$

$$\Delta\chi(t) = \int \chi^{(3)}(t-t') : |\mathbf{E}_\omega(t')|^2 dt' \tag{2.19}$$

In the dispersionless limit, the latter becomes

$$\Delta\chi(t) = \chi^{(3)} : |E_\omega(t)|^2 \tag{2.20}$$

This is a reasonable approximation when the dispersion of $\Delta\ \chi$ is negligible within the bandwidth of the field. The optical-field-induced refractive index can be defined as

$$\mathbf{\Delta n} = (2\pi/n_0)\Delta\chi \tag{2.21}$$

where n_0 is the average linear refractive index of the medium. With

$$\Delta n \equiv n_2|E_\omega|^2 \tag{2.22}$$

we obtain

$$n_2 = (2\pi/n_0)\chi^{(3)} \tag{2.23}$$

The electronic distribution in a medium can be distorted in such a way as to induce a refractive index change. Due to the field mixing with electronic wave functions shifting energy levels and redistributing populations, resonant enhancement occurs when the frequency of the beam is around an absorption band of the medium. This effect can be limited by the relaxation time for the population to readjust itself, as saturation in population redistribution can limit nonlinear effects. Despite this restriction, the response time for the electronic contribution is shorter than the molecular contributions to nonlinearity. For the sake of calculation, electronic resonance effects are ignored.

Vibrational frequencies, rotational frequencies, and molecular reorientation can also contribute the nonlinear index of refraction, but have a response time too slow to be of interest to femtosecond pulses. Highly anisotropic molecules contribute highly to the nonlinear index of refraction through stimulation of rotation frequencies. Like in the case of electronic distribution, if the beam frequency is near any resonance, the nonlinearity of the refractive index will greatly increase.

Electrostriction is a property of all dielectric materials, and is caused by the presence of randomly-aligned electrical domains within the material. When an electric field is applied to the dielectric, the opposite sides of the domains become differently charged and attract each other, reducing material thickness in the direction of the applied field, and increasing thickness in the orthogonal directions. This causes in increase in the density of the medium in that region as the molecules react to minimize the free energy of the system. The resulting strain is proportional to the square of the polarization. Because of the high magnitude of this nonlinearity compared to other causes and short response time ($\sim 10^{-16}$ s), this is the main mechanism of induced nonlinear refractive index change in this experiment, as resonances are ignored.

2.3.2 Simple Theory

This derivation follows in the lines of Cheung et. al., Gustafson et. al, and Shimizu [105] [108] [112]. We begin by considering the propagation of a laser pulse in an isotropic medium which can be described by the wave equation of a plane wave as:

$$(\frac{\delta^2}{\delta z^2} - \frac{n_0^2}{c^2}\frac{\delta^2}{\delta t^2})E = \frac{4\pi}{c^2}\frac{\delta^2}{\delta t^2}P^{(3)} \tag{2.24}$$

where

$$E = \mathcal{E}(z,t)exp(ik_0 z - i\omega_0 t) \tag{2.25}$$

$$P^{(3)} = \chi^{(3)}|E|^2 E \tag{2.26}$$

and n_0 is the linear refractive index of the medium. We then introduce the slowly varying amplitude approximation by neglecting the second order derivative of the electric field with respect to time and ignoring higher order terms on the right side of the equation from Equation (2.24) to become

$$(\frac{\delta}{\delta z} + \frac{n_0}{c}\frac{\delta}{\delta t})\mathcal{E} = -\frac{4\pi\omega_0^2}{i2k_0c^2}\chi^{(3)}|\mathcal{E}|^2\mathcal{E} \tag{2.27}$$

This approximation assumes an instantaneous response of $\chi^{(3)}$. Substituting

$$z' \equiv z + ct/n_0 \tag{2.28}$$

and

$$\mathcal{E} = |\mathcal{E}| exp(i\phi) \tag{2.29}$$

From Equation (2.27) we get

$$\frac{\delta|\mathcal{E}|}{\delta z'} = 0 \tag{2.30}$$

$$\frac{\delta\phi}{\delta z'} = \frac{2\pi\omega_0^2}{c^2 k_0}\chi^{(3)}|\mathcal{E}|^2 \tag{2.31}$$

These two equations are solved to yield

$$|\mathcal{E}| = |\mathcal{E}(t)| \tag{2.32}$$

$$\phi(z,t) = \phi_0 + \frac{2\pi\omega_0^2}{c^2 k_0}\chi^{(3)}|\mathcal{E}(t)|^2 z \tag{2.33}$$

The first of these two equations shows that the laser pulse propagates in the medium without any distortion of the pulse shape, while the latter shows that the induced phase changed

$$\Delta\phi(t) = \phi(z,t) - \phi_0 \tag{2.34}$$

is the additional phase shift experienced by the wave in its propagation from the start position to a distance z due to the presence of the induced refractive index

$$\Delta n = \frac{2\pi}{n_0}\chi^{(3)}|\mathcal{E}|^2 \tag{2.35}$$

which makes the phase change

$$\Delta\phi = (\omega/c)\int_0^z \Delta n dz \tag{2.36}$$

Since the frequency of the wave is

$$\omega = \omega_0(\delta\Delta\phi/\delta t) \tag{2.37}$$

the phase modulation $\Delta\ \phi(t)$ leads to a frequency modulation

$$\Delta\omega(t) = -\delta(\Delta\phi)/\delta t \tag{2.38}$$

$$= -\frac{2\pi\omega_0^2}{c^2 k_0}\chi^{(3)}\frac{\delta|\mathcal{E}|^2}{\delta t}z \tag{2.39}$$

The spectrum of the self-phase-modulated field is, therefore, expected to be broadened. It can be calculated from the Fourier transformation

$$|E(\omega)|^2 = |\frac{1}{2\pi}\int_{-\infty}^{\infty}\mathcal{E}(t)e^{i\omega_0 t+i\omega t}dt|^2 \tag{2.40}$$

Figure 2.4 shows this calculation for a 4.5-ps full width at half-maximum (FWHM) Gaussian laser pulse propagating in a nonlinear medium which results in a maximum phase modulation of 72π radians. In addition, Figure 2.5 shows self-phase modulation resulting in a diffraction-like pattern of broadening around the central frequency.

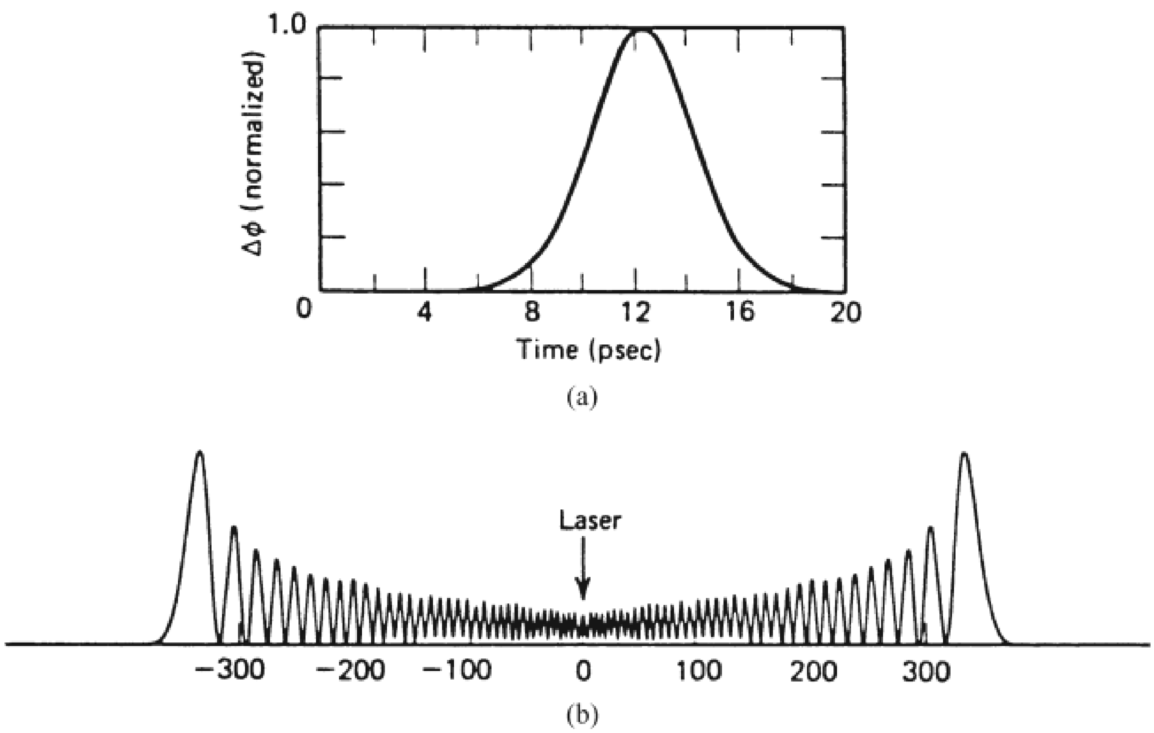

Figure 2.4: Theoretical power spectrum with an instantaneous response to intensity variation, so the phase modulation is proportion to the intensity. (a) Phase modulation verses time and (b) power spectrum of the phase-modulated pulse. Image taken from [132]

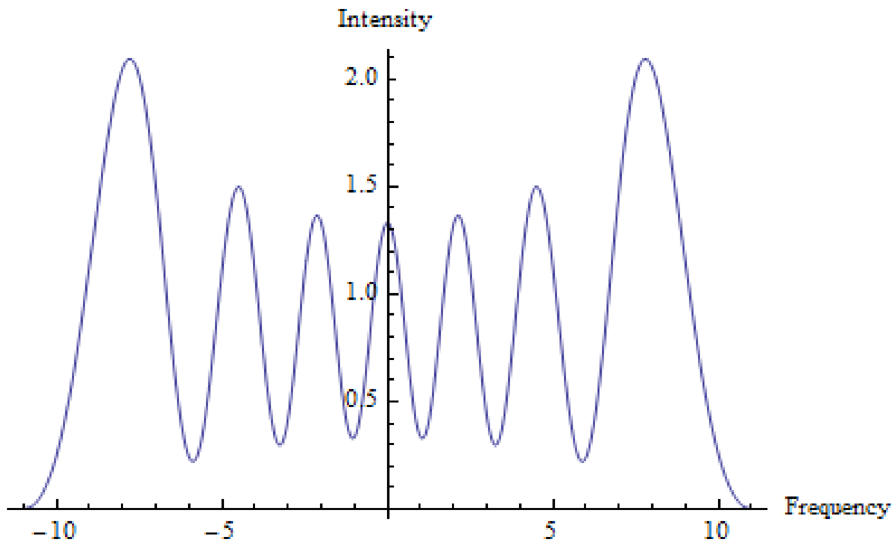

Figure 2.5: Power spectrum due to phase modulation. The pulse propagates through a shorter amount of medium than Figure 2.4.

It is interesting to note that the leading half of the phase modulation is responsible for the Stokes broadening and the lagging half for the anti-Stokes broadening. The broadened spectrum has Stokes-anti-Stokes symmetry because the phase modulation is directly proportional to the intensity and the pulse is symmetric. Because the frequency is the derivative of the phase modulation with respect to time, points of constant slope on the phase modulation curve describe radiated waves of the same frequency but different phases. Depending on how separated in time the two waves of constant frequency are, they interfere either constructively or destructively. This behavior is shown in the interference pattern of the power spectrum. The inflection points have the largest slope on the phase modulation curve and lead to the two outermost peaks on the power spectrum. The number of pairs of constructive and destructive interferences is $\phi_{max}/2\pi$ on each side of the spectrum.

Because the response of the medium to the laser pulse is not instantaneous, we introduce the terms

$$\Delta\phi(z,t) = (\omega/c)\int_0^z \Delta n(z,t)dz \tag{2.41}$$

and

$$\Delta n(z,t) = \int_{-\infty}^{z} n_2(z, t-t')|E(z,t')|^2 dt' \tag{2.42}$$

In this condition, even if the intensity is symmetric, the phase modulation is not. This is a result of Stokes-anti-Stokes asymmetry. The Stokes side of the spectrum is always stronger because the leading edge of the phase modulation curve always sees a larger portion of the intensity pulse. Figure 2.6 shows this calculation again in the case of finite response time. This approximation is a good start in our case, because in the case of an optical fiber, the transverse beam profile SPM is suppressed from the waveguide.

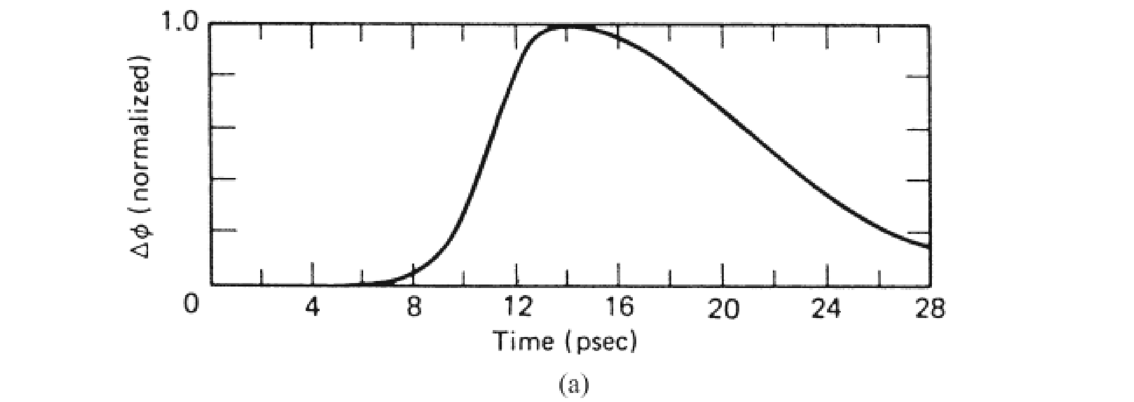

Figure 2.6: Theoretical power spectrum in the case of finite response time. (a) Phase modulation verse time and (b) power spectrum of the phase-modulated pulse. Image taken from [132]

2.3.3 More complicated SPM theory

This derivation of SPM will assume a thin medium in which there is no self-focusing effect of SPM and the transient stimulated light-scattering processes are suppressed. This analysis follows in the case of Fork et. al. in which a 80-fs pulse at 627 nm focusing to an intensity of 1013 to 1014 W/cm on a 500-μm film of ethylene glycol [117]. The output was observed as a white continuum with a huge spectral broadening from the input.

The simplification we applied in Equation (2.27) will be revised as these terms will be reinstated. The effect of this will be the inclusion of the self-steepening effect of the pulse that was not present in the simple theory. From Equation (2.24) the field amplitude is [115]:

$$(\frac{\delta}{\delta z} + \frac{n_0}{c}\frac{\delta}{\delta t})\mathcal{E} + \frac{1}{i2k_0}(\frac{\delta^2}{\delta z^2} - \frac{n_0^2}{c^2}\frac{\delta^2}{\delta t^2})\mathcal{E} \tag{2.43}$$

$$= -\frac{4\pi\omega_0^2}{i2k_0c^2}\chi^{(3)}|\mathcal{E}|^2\mathcal{E} + \frac{2\pi}{ik_0c^2}(-i2\omega_0\frac{\delta}{\delta t} + \frac{\delta^2}{\delta t^2})\chi^{(3)}|\mathcal{E}|^2\mathcal{E} \tag{2.44}$$

We then define the differential operators as

$$D_\pm \equiv (\delta/\delta z) \pm (n_0/c)(\delta/\delta t) \tag{2.45}$$

and rewrite Equation (2.44) as

$$D_+\mathcal{E} + \frac{1}{i2k_0}D_-D_+\mathcal{E} = \frac{1}{i2k_0}\Pi \tag{2.46}$$

$$\Pi = -\frac{4\pi\omega_0^2}{c^2}[1 + \frac{2i}{\omega_0}\frac{\delta}{\delta t} - \frac{1}{\omega_0^2}\frac{\delta^2}{\delta t^2}]\chi^{(3)}|\mathcal{E}|^2\mathcal{E} \tag{2.47}$$

Since

$$D_- = -(2n_0/c)(\delta/\delta t) + D_+ \tag{2.48}$$

we have

$$D_+\mathcal{E} = \frac{1}{i2k_0}[(-\frac{2n_0}{c}\frac{\delta}{\delta t} + D_+)D_+\mathcal{E} + \Pi] \tag{2.49}$$

$$= \frac{1}{i2k_0}\sum_{m=0}^{\infty}[(-\frac{2n_0}{c}\frac{\delta}{\delta t} + D_+)/i2k_0]^2\Pi \tag{2.50}$$

We then have to decide how many terms in the power series expansion is appropriate to describe SPM. The zeroth-order approximation corresponds to neglecting all derivatives and yields

$$D_+\mathcal{E} = -(2\pi\omega_0^2/ic^2k_0)\chi^{(3)}|\mathcal{E}|^2\mathcal{E} \tag{2.51}$$

which is what we had in Equation (2.27). For this lowest order approximation,

$$D_+(\chi^{(3)}|\mathcal{E}|^2\mathcal{E}) \propto (\chi^{(3)}|\mathcal{E}|^2)^2\mathcal{E} \tag{2.52}$$

$$\ll \chi^{(3)}|\mathcal{E}|^2\mathcal{E} \tag{2.53}$$

if

$$\chi^{(3)}|\mathcal{E}|^2 \ll 1 \tag{2.54}$$

We can therefore use D^+ as an expansion parameter in the higher-order calculations. For the first-order approximation, we have

$$D_+\mathcal{E} = \frac{1}{i2k_0}\sum_{m=0}^{\infty}[(\frac{1}{i\omega_0}\frac{\delta}{\delta t})^m\Pi] \tag{2.55}$$

$$= (1+\frac{1}{\omega_0}\frac{\delta}{\delta t})[-\frac{2\pi\omega_0^2}{ik_0c}\chi^{(3)}|\mathcal{E}|^2\mathcal{E}|] \tag{2.56}$$

In a sense we have used $\chi^{(3)}|\mathcal{E}|^2$ as the expansion parameter, neglecting any orders higher than one of this term. For the case of an ultrashort pulse in a condensed medium, even if the laser pulse intensity is $10^{14}W/cm^2$, we find

$$\chi^{(3)}|\mathcal{E}|^2 \sim 4x10^3 \ll 1 \tag{2.57}$$

Therefore, the approximation seems to be a reasonably good one.

Taking the nonlinear index of refraction as

$$n_2 = (2\pi\omega_0)/k_0c)\chi^{(3)} \tag{2.58}$$

we then have

$$\frac{\delta\mathcal{E}}{\delta z} + \frac{1}{c}\frac{\delta}{\delta t}(n_0\mathcal{E} + n_2|\mathcal{E}|^2) = i\frac{n_2\omega_0}{c}|\mathcal{E}|^2\mathcal{E} \tag{2.59}$$

We now take the simplification of assuming an instantaneous response of the medium. By neglecting the dispersion of the response of the medium, we obtain

$$[\frac{\delta}{\delta z}+\frac{n_0}{c}(1+\frac{3n_2}{n_0}|\mathcal{E}|^2)\frac{\delta}{\delta t}]|\mathcal{E}|=0 \tag{2.60}$$

$$[\frac{\delta}{\delta z}+\frac{n_0}{c}(1+\frac{n_2}{n_0}|\mathcal{E}|^2)\frac{\delta}{\delta t}]\phi=\frac{n_2\omega_0}{c}|\mathcal{E}|^2 \tag{2.61}$$

The former equation describes the amplitude of the wave, while the latter describes the phase. By comparing this equation to Equation (2.31) from the simple theory of SPM, the only difference is the addition of the $n_2|\mathcal{E}|^2$ terms on the left-hand side. When $\Delta n > 0$, we expect a pulse steepening in the lagging edge. This is because the peak of the pulse then propagates at a lower velocity than either the leading or the lagging part of the part.

With a pulse of the form

$$|\mathcal{E}(0,t)|^2 = A^2/cosh(t/\tau) \tag{2.62}$$

the solution of Equation (2.61) becomes

$$\phi = \omega_0\tau(x - sinh^{-1}[sinhx - (n_2/c\tau)A^2z]) \tag{2.63}$$

where

$$x = [t - (n_0/c)z]/\tau \tag{2.64}$$

and the frequency modulation is

$$\Delta\omega/\omega_0 = [1 + (Q^2 - 2Qsinhx)/coshx]^{-1/2} - 1 \tag{2.65}$$

where

$$Q = n_2A^2z/c\tau \tag{2.66}$$

As shown in Figure 2.7, the spectral broadening actually results from frequency chirping. Because of the inclusion of the $\chi^{(3)}$ term, this solution takes into account all third order phenomena, including the four-wave mixing contributions.

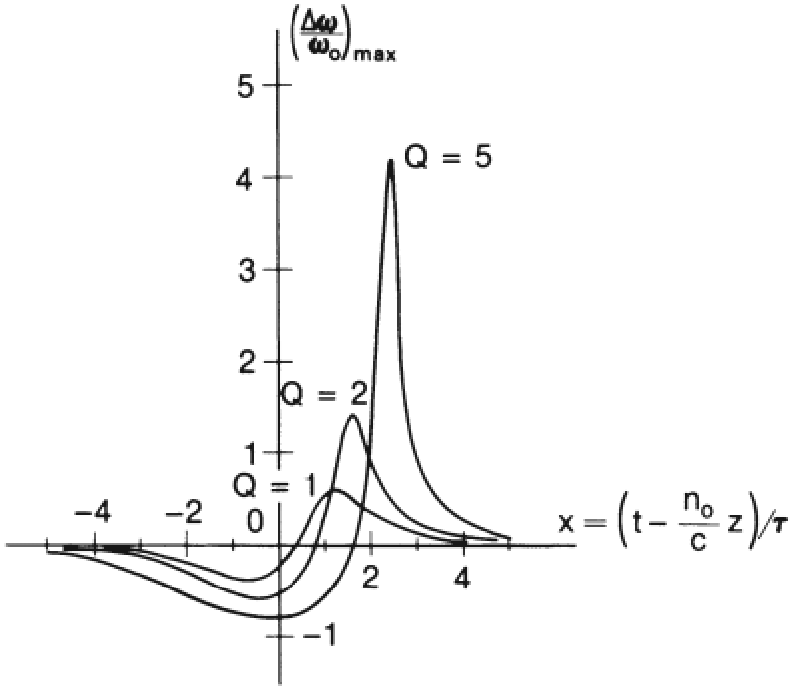

Figure 2.7: Frequency shift due to phase modulation as a function of $x = (t - n_0 z/c)/\tau$ at various values of $Q = n_2 A^2 zc/\tau$. Image taken from [132].

2.4 Dispersion

We begin our discussion of dispersion within optical fibers by considering Maxwells equations within a nonmagnetic medium as

$$\nabla \times \nabla \times \mathbf{E} = -\mu_0 \frac{\delta^2 \mathbf{D}}{\delta t^2} \tag{2.67}$$

where $\mathbf{E}$ is the electric field, μ_0 is the vacuum permeability, and $\mathbf{D}$ is the electric flux density. The relation between $\mathbf{D}$ and $\mathbf{E}$ in the frequency domain can be written as

$$\tilde{\mathbf{D}}(\mathbf{r}, \omega) = \varepsilon_0 \tilde{n}^2 \tilde{\mathbf{E}}(\mathbf{r}, \omega) \tag{2.68}$$

where ε_0 is the vacuum permittivity, $\tilde{n}$ is the refractive index, and $\tilde{\mathbf{E}}$ and $\tilde{\mathbf{D}}$ are the Fourier transforms of $\mathbf{E}$ and $\mathbf{D}$ respectively, that is

$$\tilde{\mathbf{E}}(\mathbf{r}, \omega) = \frac{1}{2\pi} \int_{-\infty}^{\infty} \mathbf{E}(\mathbf{r}, t) exp(i\omega t) dt \tag{2.69}$$

with a similar relation for $\tilde{\mathbf{D}}(\mathbf{r}, \omega)$. Using Equations (2.67)-(2.69), we obtain

$$\nabla^2 \tilde{\mathbf{E}} + (\tilde{n}\omega/c)^2 \tilde{\mathbf{E}} = 0 \tag{2.70}$$

where we have assumed that $\nabla \mathbf{E} \cong 0$. The refractive index in optical fibers is given by

$$\tilde{n} = n(\mathbf{r}, \omega) + i\alpha c/2\omega + n_2|\mathbf{E}|^2 \tag{2.71}$$

The linear index $n(\mathbf{r}, \omega)$ in this case is not constant in the transverse dimensions to account for dielectric waveguiding. To account for the chromatic dispersion in silica fibers, the index of refraction is also frequency dependent. The coefficient α reflects the fiber loss. The n_2 term takes into account the nonlinear component, referred to as the optical Kerr effect.

Assuming a homogenous fiber composition along the length of the fiber (z direction) in such a way that the index of refraction is constant with respect to z, we assume:

$$\tilde{\mathbf{E}}(x, y, z, \omega) = \hat{e}\tilde{a}(z, \omega)\psi(x, y) = \hat{e}E_0\psi(x, y)exp(i\tilde{\beta}z) \tag{2.72}$$

where $\hat{e}$ is the polarization unit vector, $\tilde{\beta}$ is the wave number and $\psi(x, y)$ is obtained by solving

$$\frac{\delta^2\psi}{\delta x^2} + \frac{\delta^2\psi}{\delta y^2} + (\frac{\tilde{n}^2\omega^2}{c^2} - \tilde{\beta}^2)\psi = 0 \tag{2.73}$$

Since the last two terms in Equation (2.71) are much smaller than the linear index $n(x, y, \omega)$, they can be treated by first-order perturbation theory. The complex wave number $\tilde{\beta}$ can be approximated by

$$\tilde{\beta} \cong \beta(\omega) + i\alpha/2 + \Delta\beta_{NL} \tag{2.74}$$

where

$$\Delta\beta_{NL} = \frac{n_2\omega}{c} \int \int_{\sigma} |\psi(x, y)|^2 |\mathbf{E}|^2 dxdy \tag{2.75}$$

and where σ represents the fiber cross section and $\beta(\omega)$ is obtained by solving the eigenvalue equation

$$\frac{\delta^2\psi}{\delta x^2} + \frac{\delta^2\psi}{\delta y^2} + (n(x, y, \omega)\frac{\omega^2}{c^2} - \beta^2(\omega))\psi = 0 \tag{2.76}$$

for a given index distribution of the fiber. For a single mode fiber, the field distribution $\psi(x,y)$ must satisfy the normalization conditions

$$\int\int_{\sigma} |\psi(x,y)|^2 dxdy = 1 \tag{2.77}$$

The envelope propagation equation can be found from Equations (2.72) and (2.74) to yield

$$\frac{\delta \tilde{a}}{\delta z} = i[\beta(\omega) + i\alpha/2 + \Delta\beta_{NL}]\tilde{a} \tag{2.78}$$

Since the pulse spectrum is centered at the carrier frequency ω_0, we can expand the wave number in a Taylor series about the carrier frequency as

$$\beta(\omega) = \beta_0 + (\omega - \omega_0)\beta_1 + \frac{1}{2}(\omega - \omega_0)^2\beta_2 + \frac{1}{6}(\omega - \omega_0)^3\beta_3 \tag{2.79}$$

where $\beta_0 = d^n\beta/d\omega^n$ is evaluated at ω_0. The coefficient β_0 represents the phase velocity, which is the velocity at which the phase of any one frequency component of the wave travels. The group velocity $v_g = 1/\beta_1$ is the velocity at which the pulse envelope moves at. The group velocity dispersion (GVD) is given by β_2. We then find the slowly varying pulse amplitude as

$$a(z,t) = A(z,t)exp[i(\beta_0 z - \omega_0 t)] \tag{2.80}$$

where $a(z,t)$ is the inverse Fourier transform of $\tilde{a}(z,\omega)$. During the Fourier transform, the differential operator $i(\delta/\delta t)$ replaces $(\omega\omega_0)$. A combination of Equations (2.78)-(2.80) then yields the propagation equation

$$\frac{\delta A}{\delta z} + \beta_1\frac{\delta A}{\delta t} + \frac{\alpha}{2}A + \frac{i}{2}\beta_2\frac{\delta^2 A}{\delta t^2} - \frac{1}{6}\beta_3\frac{\delta^3 A}{\delta t^3} = i\gamma|A|^2 A \tag{2.81}$$

where the nonlinearity coefficient

$$\gamma = n_2\omega_0/cA_{eff} \tag{2.82}$$

The parameter A_{eff} is known as the effective fiber core area and is given by

$$A_{eff}^{-1} = \int\int_{\sigma} |\psi(x,y)|^4 dxdy \tag{2.83}$$

where $E = A\psi$.

Equation (2.81) describes the propagation of an optical pulse in single-mode fibers. While both material dispersion and waveguide dispersion contribute to the group velocity dispersion, the material dispersion contribution is generally larger. We can therefore approximate β_2 as

$$\beta_2 \simeq (\lambda/2\pi c^2)D(\lambda) \tag{2.84}$$

where

$$\lambda = 2\pi c/\omega_0 \tag{2.85}$$

and

$$D(\lambda) = \lambda^2(d^2n/d\lambda^2) \tag{2.86}$$

For the sake of completeness, we now consider the effect of stimulated Raman scattering (SRS), which has been thus far ignored. For ultrashort femtosecond optical pulses, the pulse spectrum is wide enough that the low-frequency components get amplified from the Raman gain at the expense of the high-frequency components. As a result, the spectrum shifts toward shorter frequencies as the pulse propagates inside the fiber [118] [119]. The resulting propagating equation including this effect and the SRS effect is [120]

$$\frac{\delta A}{\delta z} + \beta_1\frac{\delta A}{\delta t} + \frac{\alpha}{2}A = -\frac{i}{2}\beta_2\frac{\delta^2 A}{\delta t^2} + i\gamma|A|^2A + \frac{1}{6}\beta_3\frac{\delta^3 A}{\delta t^3} \tag{2.87}$$

$$-a_1\frac{\delta}{\delta t}(|A|^2A) - a_2A\frac{\delta|A|^2}{\delta t} \tag{2.88}$$

Because of the low powers used in this experiment, we will ignore the SRS effects [121].

2.5 Self-phase modulation plus dispersion

Depending on the ratio of the dispersion length L_D and the nonlinear length L_{NL}, the propagation of the beam within the fiber is characterized by different regimes. We will define the dispersion length as

$$L_D = T_0^2/|\beta_2| \tag{2.89}$$

and we will define the nonlinear length as

$$L_{NL} = (\gamma P_0)^{-1} \tag{2.90}$$

where T_0 and P_0 are related to the width and the peak power of the incident pulse. We can rewrite Equation (2.81) in a more convenient form

$$i\frac{\delta U}{\delta z} = \pm\frac{1}{2L_D}\frac{\delta^2 U}{\delta \tau^2} - \frac{1}{L_{NL}}e^{-\alpha z}|U|^2 U \tag{2.91}$$

where we have defined

$$\tau = (t - \beta_1 z)/T_0 \tag{2.92}$$

and

$$A = \sqrt{P_0} exp(-\alpha z/2)U \tag{2.93}$$

The dispersion-dominant regime is where the fiber length is much less than the nonlinear length, but comparable to the dispersion length. The equation determining behavior in this regime is obtained by solving Equation (2.91) as

$$U(z,\tau) = \int_{-\infty}^{\infty} \tilde{U}(0,\omega) exp[-i\omega\tau \pm i\omega^2(z/2L_D)]d\omega \tag{2.94}$$

where $\tilde{U}(0,\omega)$ is the Fourier transform of the incident pulse amplitude. The dynamics of this regime were extrapolated by Marcuse, but are not of importance to this experiment [122]. The nonlinearity-dominant regime is where the fiber length is much smaller than the dispersion length but on the order of or larger than the nonlinear length. This situation in described in the previous section.

The regime in which we are interested in this experiment is the dispersive nonlinear regime, characterized in which the fiber length is longer than or comparable to both the dispersion length and the nonlinear length. In this regime, both dispersion and nonlinear effects act together on the pulse during propagation. This derivation follows in the lines of Mollenauer et. al., Grischowsky and Balant, and Tomlinson et. al., in which the numerical solutions were in high agreement with experimental results [123] [124] [125].

We begin by normalizing the fiber length as

$$\xi = z/L_D \tag{2.95}$$

so that Equation (2.91) can be written as

$$i\frac{\delta U}{\delta \xi} = \pm\frac{1}{2}\frac{\delta^2 U}{\delta \tau^2} - N^2 e^{-\alpha z}|U|^2 U \tag{2.96}$$

where

$$N^2 = \frac{L_D}{L_{NL}} = \frac{\gamma P_0 T_0^2}{|\beta_2|} \tag{2.97}$$

In the lossless case, Equation (2.96) is analogous to the nonlinear Schrodinger equation (NLSE). In the case when the GVD parameter $\beta_2 < 0$, referred to as the anomalous dispersion regime, the NLSE has exact solutions, referred to as solitons [126] [127]. For a hyperbolic secant initial pulse shape and integer values of N, the solitons follow a periodic evolution pattern of period

$$z_0 = \frac{\pi}{2}L_D = \frac{\pi T_0^2}{2|\beta_2|} \tag{2.98}$$

The fundamental soliton corresponds to N = 1 and propagates without change in its shape. The peak power required to excite this soliton is

$$P_1 = |\beta_2|/\gamma T_0^2 \tag{2.99}$$

Numerical solutions to Equation (2.96) give proper simulation of the parameters of this experiment. A fast Fourier transform (FFT) based beam propagation method is used as was used in similar experiments [128] [129] [130]. This consists in propagating the field a distance $\delta/2$ with dispersion only, multiplying the result by a nonlinear term that represents the effect of nonlinearity over the whole step length δ, and then propagating the field for the remaining distance $\delta/2$ with dispersion only. It is useful to write Equation (2.96) in the form

$$\frac{\delta U}{\delta \xi} = (D + Q)U \tag{2.100}$$

where

$$D = \pm\frac{i}{2}\frac{\delta^2}{\delta\tau^2} \tag{2.101}$$

and

$$Q = iN^2 e^{-\alpha z}|U|^2 \tag{2.102}$$

The field is propagated inside the fiber a small distance δ by

$$U(\xi+\delta,\tau) = [exp(\frac{\delta D}{2})exp(\int_{\xi}^{\xi+\delta} Q(\xi')d\xi')exp(\frac{\delta D}{2})]U(\xi,\tau) \tag{2.103}$$

The propagation in a linear dispersive medium indicated by the exponential operator $exp(\delta D/2)$ can be accomplished using the Fourier transform method. This integral is approximated with the trapezoidal rule as

$$\int_{\xi}^{\xi+\delta} Q(\xi')d\xi' \simeq \frac{1}{2}\delta[Q(\xi)+Q(\xi+\delta)] \tag{2.104}$$

This can further be approximated as

$$\int_{\xi}^{\xi+\delta} Q(\xi')d\xi' \simeq \delta[Q(\xi)] \tag{2.105}$$

as long as the intensity of the field does not significantly change from one step to the next.

The propagation for a pulse modeled by these equations, and the spectrum resulting is shown in Figure 2.8. Of interest are the oscillations near the pulse edges, which are manifest in the spectrum as sidelobes. This is often referred to as wave-breaking, interpreted by Tomlinson et. al. as a mixing of the SPM induced frequency-shifted components with the unshifted light in the wings [131].

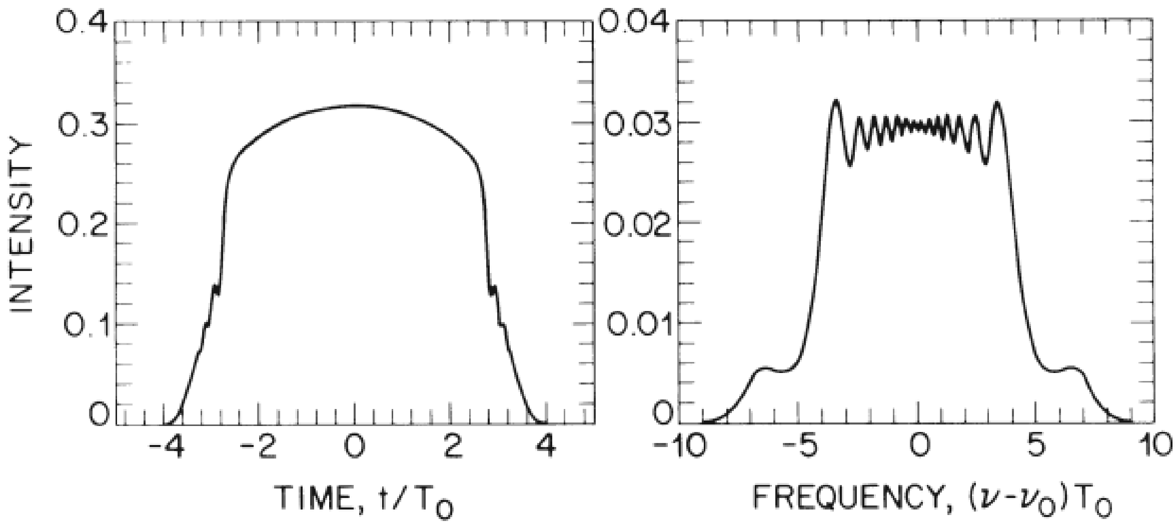

Figure 2.8: Pulse shape and spectrum of an unchirped Gaussian pulse at $\xi = 0.08$ for N = 30. Sidelobes in the spectrum and oscillations near the pulse edges are due to optical wave breaking. Image taken from [132].

CHAPTER 3

DATA

We solve the problems produced from modulation instability by using a ultra high numerical aperture (UHNA) optical fiber, leading to increased shot-to-shot stability, allowing it to be used effectively in multiphoton microscopy (MPM). We examine the three measurements made in this experiment, shot-to-shot stability, spectral characterization, and the use of this light in nonlinear microscopy. The continuum generation was done in the normal dispersion regime with the high NA fiber.

3.1 Shot-to-shot Stability

We used a $Yb : KGd(WO_4)_2$ laser at 19 MHz to generate 250 fs pulses used in the experiment. This was then sent through a beam expander of 1.25x, using lenses of 200mm and 250mm in order to optimize the input to the fiber optic acceptor. The fiber used was a CoreActive, SCF-UN-3/125-25-PM optical fiber. It contained 1 cm of entrance fiber containing 6.7 μm core diameter which was coupled to 2.15 m of polarization maintaining (PM) 3 μm core ultra high numerical aperture (UHNA) fiber. The numerical aperture (NA) is defined as the index of refraction times the sine of the half angle of incidence. The entrance fiber allowed for easier alignment, and because of its lower NA, it was able to accept a larger range of input angles to the fiber. The NA for this section is 0.25. The clad diameter for the PM fiber was 126 μm, which was one micron too large for the output connector. Therefore, 1 cm of exit fiber was added, which had a core diameter of 6.7 μm. A photodiode was used at the input of the fiber originally, and then was moved to the output of the fiber to measure the shot-to-shot stability through the fiber. This experimental setup is shown in Figure 3.1. As shown in Figure 3.2, this experiment had complete shot-to-shot stability. This is a large advantage for reliable use in nonlinear microscopy. If there is not reliable shot-to-shot stability, the dwell time must be increased to be able to average out the variations for use in microscopy. An increase of dwell time not only increases the overall time required to take a sample, but also increases the chance of photobleaching or photodamage occurring in biological samples. By having complete shot-to-shot stability in a regime that does not amplify noise, microscopy becomes more accurate and faster.

The previous experiment performed by Field et. al. showed extremely intermittent shot-to-shot behavior [93]. Due to the noise instability, and hence frequency modulation, the output for dMPLSM was not temporally coherent enough to perform adequate SHG microscopy.

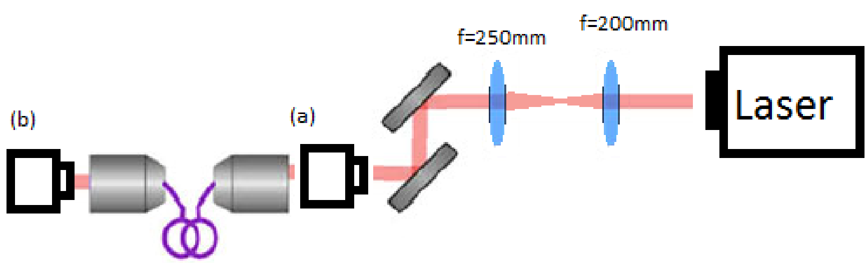

Figure 3.1: Experimental setup to measure shot-to-shot stability. The photodiode was originally placed (a) before the fiber, then was moved to (b) after the fiber.

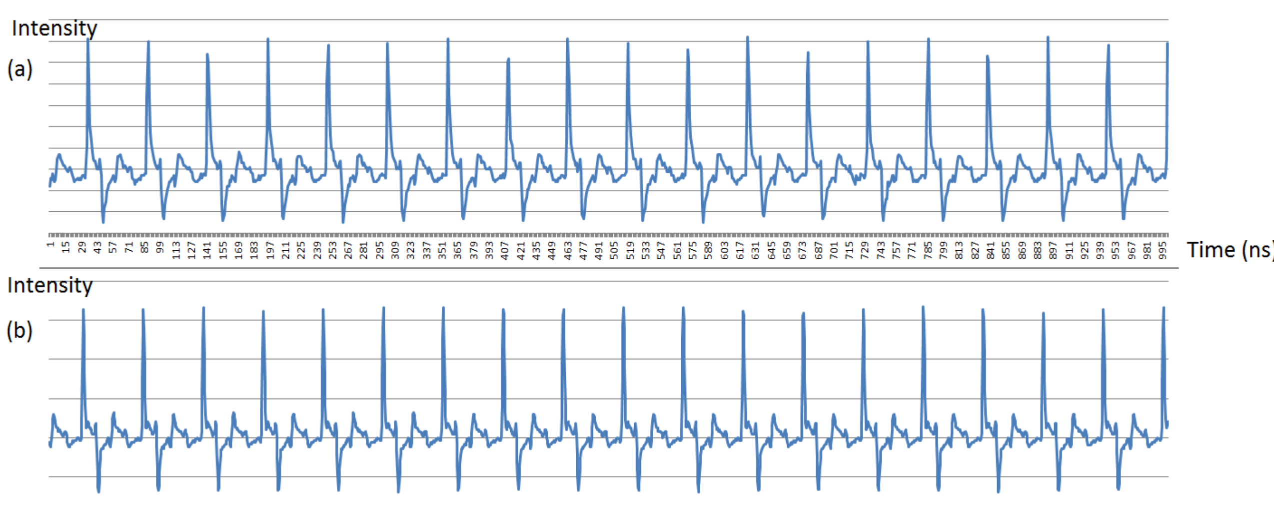

Figure 3.2: Comparison of shot-to-shot stability (a) before and (b) after the fiber.

3.2 Spectral Characterization

For the spectral characterization, the setup was changed so that the output from this fiber was sent into a spectrometer and the output was recorded on a charge-coupled device (CCD) camera. Because of the bandwidth of the output spectra, multiple pictures had to be put together to capture the complete spectra at one setting. Because the CCD camera automatically adjusted to the intensity in each picture, stitching of the pictures sometimes resulted in abrupt changes in the measured spectra. Background noise is caused by room lights contributing to the spectra. The experimental setup is shown in Figure 3.3. Differentiation of the polarization axes was determined by looking at the bandwidth of the resulting spectra. The polarization axis with the least bandwidth output from the fiber was determined to be the slow axis, while the axis 90 ° from this, which had the largest bandwidth output, was determined to be the fast axis. The difference between the spectra from the two axes shows the birefringence of the fiber. The input power was between 119-202 mW, and the output power was between 15.6-24.7 mW, leading to a coupling efficiency through the fiber of 12.2-13.1%.

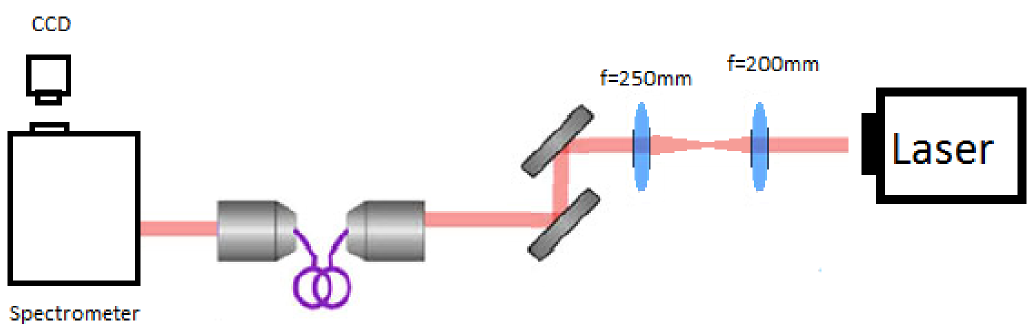

Figure 3.3: Experimental setup of the spectra from the fiber.

3.2.1 Slow Axis

Figure 3.4 shows the spectra from the mode-locked $Yb : KGd(WO_4)_2$ laser cavity, without any nonlinear effects. The output spectra from an input polarization on the slow axis is given in Figure 3.5. The bandwidth spread is roughly 27nm. At least one mode to each side can be easily identified, which has been created from SPM.

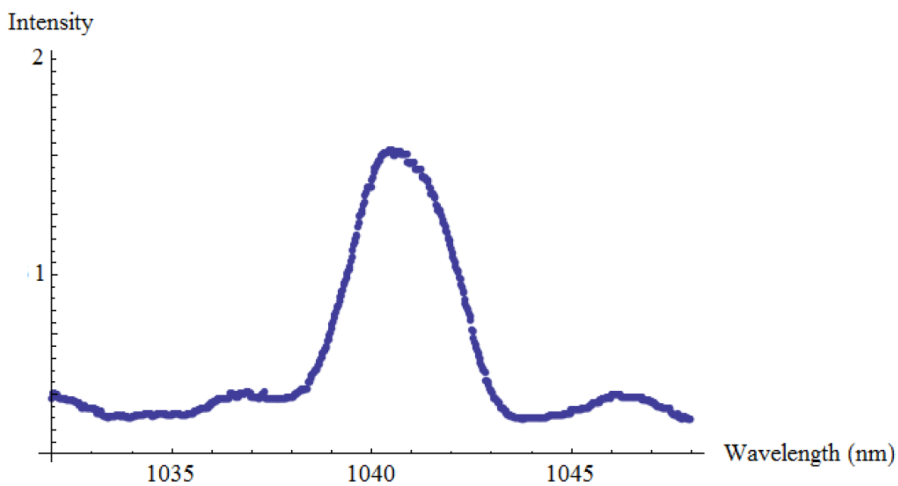

Figure 3.4: Spectra from the mode-locked $Yb : KGd(WO_4)_2$ laser cavity.

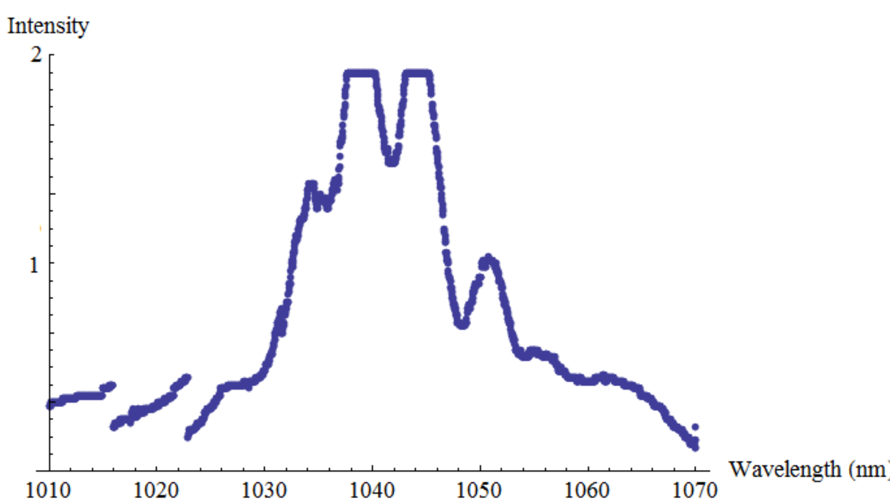

Figure 3.5: Spectra on the slow axis at 23.4 mW. The camera becomes saturated at high intensities, as can be seen by the two plateaus.

3.2.2 Fast Axis

The output spectra from an input polarization on the fast axis is given in Figure 3.6. The bandwidth spread is roughly 32nm. This is larger than the measured bandwidth spread on the slow axis, showing that the nonlinearity is greater on this axis. In addition, more modes can be seen than on the slow axis, showing the larger effect of SPM on the fast axis.

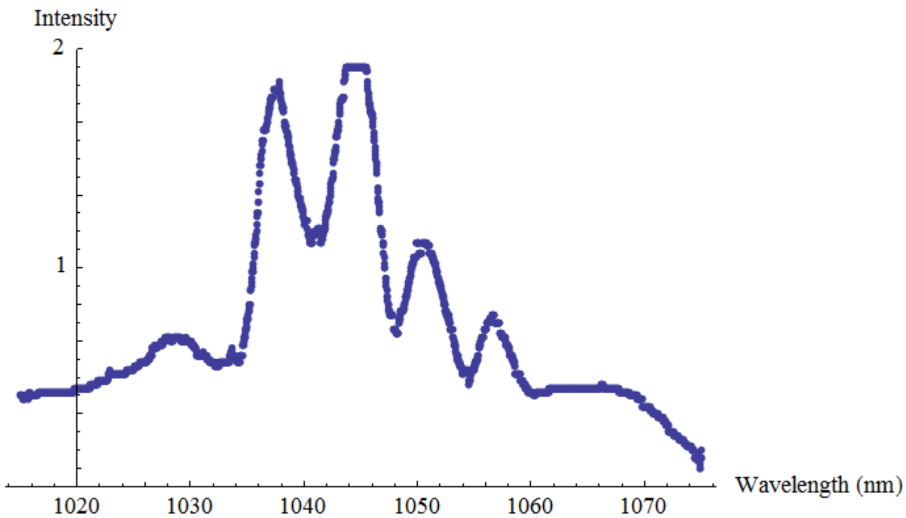

Figure 3.6: Spectra on the fast axis at 23.4 mW. The camera becomes saturated at high intensities, as can be seen by the plateau.

3.2.3 Other Polarization States

According to Lehtonen, et. al., polarization spectra in between the fast and slow axes is a weighted superposition of the propagation on the fast axis and propagation on the slow axis [62]. Figure 3.7 shows the measured spectra for various input polarizations.

3.2.4 Dependence on Input Power

The output spectra on the fast axis and slow axis at different input powers is given in Figure 3.8. This shows the third order nonlinearity in the fiber reflected in the power dependence of bandwidth spread.

3.3 Nonlinear Microscopy

The setup was changed so that the output from the fiber was put through a beam compressor of 1.875x, using lenses of 750mm and 400mm in order to reduce the spot size to maximize SHG. This beam was then sent into a SHG microscope and was used to image a

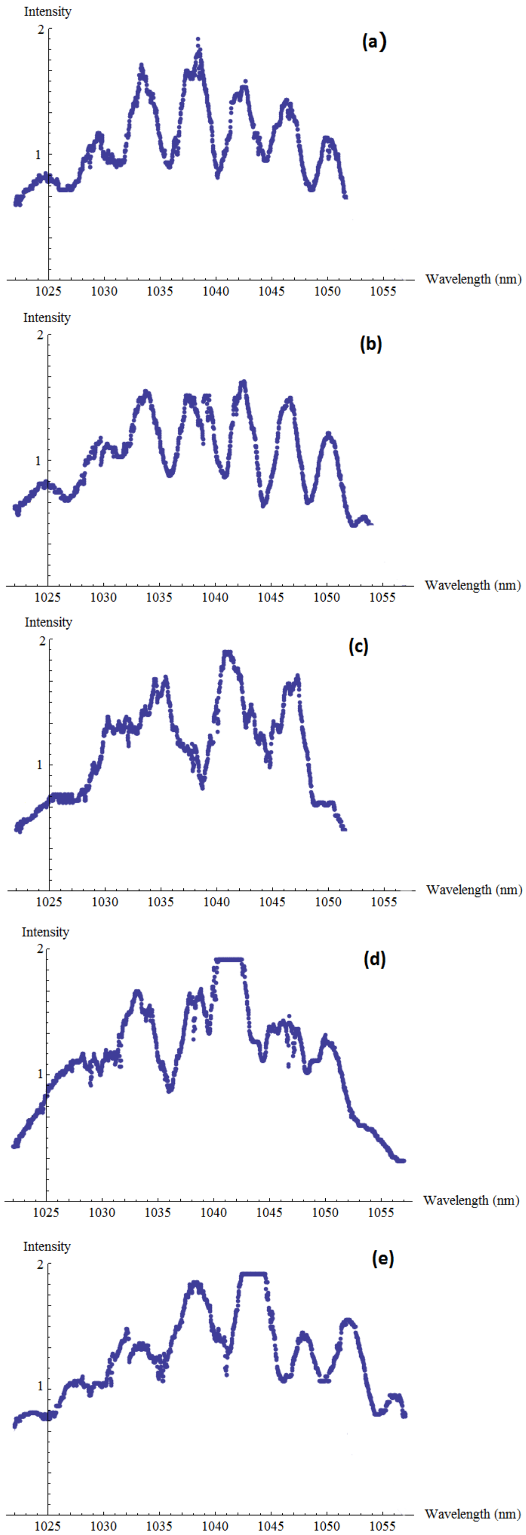

Figure 3.7: Spectra at continuously changing polarization states from (a) 14° before the slow axis to (e) 24° before the fast axis.

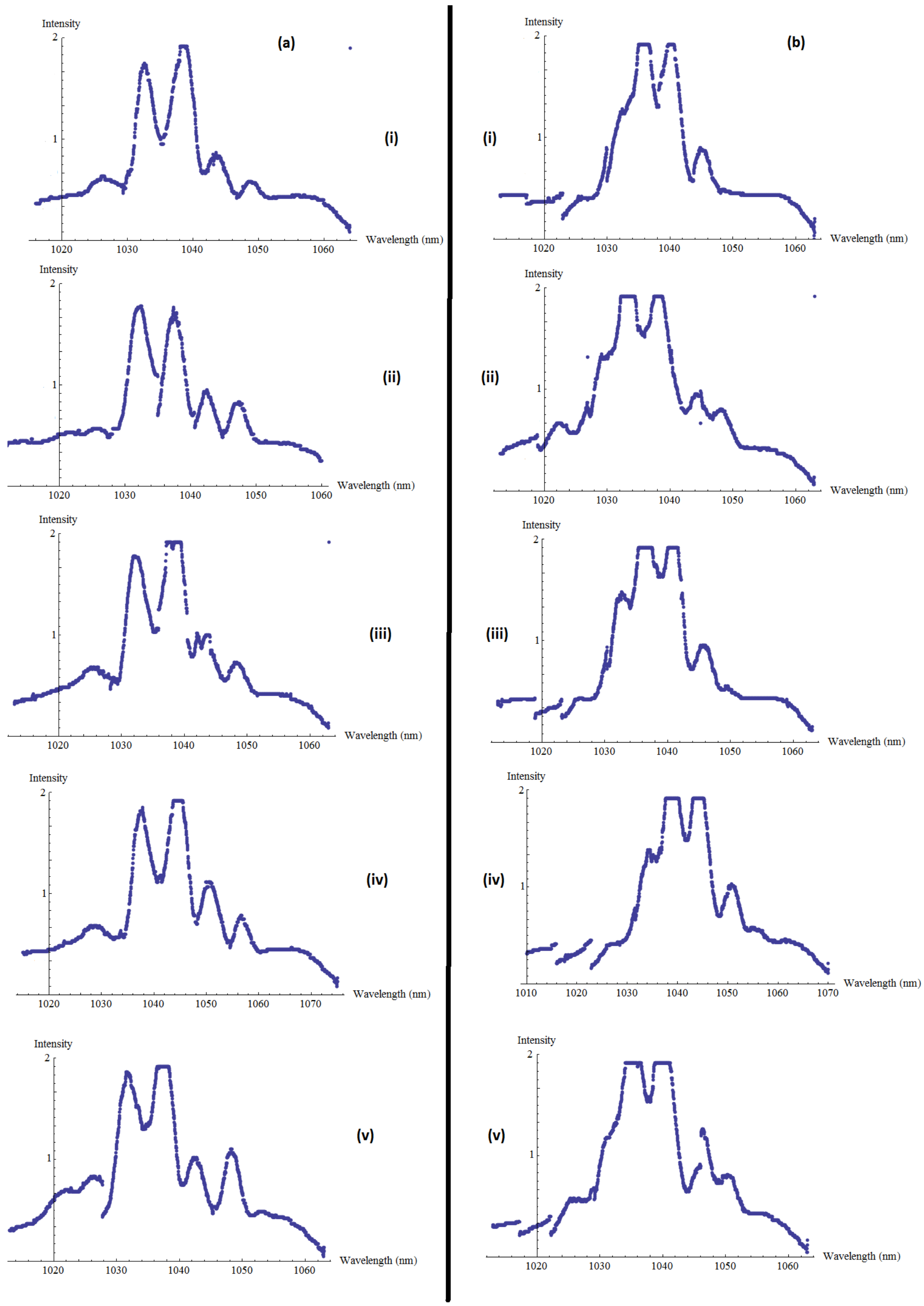

Figure 3.8: The output spectra on (a) the fast axis and (b) the slow axis. The input powers are (i) 17.8 mW, (ii) 19.6 mW, (iii) 21.7 mW, (iv) 23.4 mW, and (v) 24.7 mW.

sample of corn starch. Total power to reach the sample of corn starch was about 5mW. This setup is shown in Figure 3.9. Figure 3.10 shows the working detail of the SHG microscope. The objective used in this experiment is a 0.75 NA, 11 mm working distance (WD) objective that is not corrected for spherical abberation (SA). The corn starch sample was scanned through a coverslip, so SA was added that was not corrected for, decreasing the signal-to-noise ratio. The microscope allows for both specimen scanning and beam scanning of a sample, which creates a field of view on the order of square millimeters, which is roughly an order of magnitude larger than comparable systems. The spot size through the objective is given by

$$\frac{0.61\lambda}{NA} = 846nm \tag{3.1}$$

This microscope applies the technique of photon counting in order to render an image. This works by collecting the photon counts in a photomultiplier tube (PMT) to amplify the signal. The output from the PMT is then sent to a comparator circuit that eliminates the signals that are below the noise threshold. Finally, these counts are sent to a field programmable gate array (FPGA) which performs the counting of the photons. The image is then rendered by showing the contrast of number of counts per pixel scanned over.

The reason for the high signal to noise ratio is the temporal dispersion that the pulse experiences through the fiber. This in turn reduces the peak intensity, and the multiphoton advantage. We can estimate the temporal diffusion as analogous to the dispersion experienced through fused silica. In this case, the temporal dispersion is calculated for a gaussian pulse as

$$\tau(L) = \tau_0\sqrt{1 + (\frac{8aLln2}{\tau_0^2})^2} = 1.08ps \tag{3.2}$$

where τ_0 is 250 fs, L is 215 mm, and $a = 22$ for BK7 glass. Assuming the temporal dispersion scales linearly with bandwidth, and that the pulse through the fiber is approximately 25 nm, while the input pulse is 3 nm, we multiply this result by (25/3). This leads to a output pulse length of roughly 9 ps. By comparison with the input pulse, the exit pulse has been temporally stretch by about 36 times, leading to a degredation of peak intensity by a factor of roughly 36, and a signal to noise ratio increase of about $1.3x10^3$.

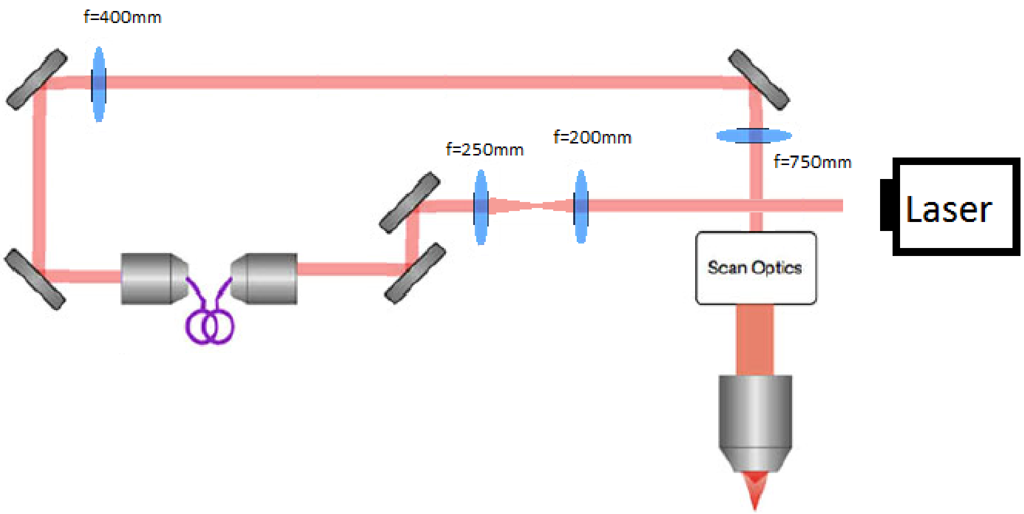

Figure 3.9: Experimental setup for SHG microscopy.

3.3.1 BG39 Filter

The results for a BG39 filter are shown in Figure 3.11. The BG39 filter allows through a wide range of wavelengths, and for our experiment, it acts mostly just to block the fundamental wavelengths between the range of 900-1200nm.

3.3.2 Filter 520-10

The results for a filter of only wavelengths between 515-525 nm are shown in Figure 3.12. Corn starch is experimentally known not to have any fluorescence, as an attenuation of fluorescence would be a possible explanation for the lower signal to noise ratio. Instead, I propose that the lower signal to noise ratio is showing that a significant amount of SHG is from the wavelengths below 515nm and above 525nm.

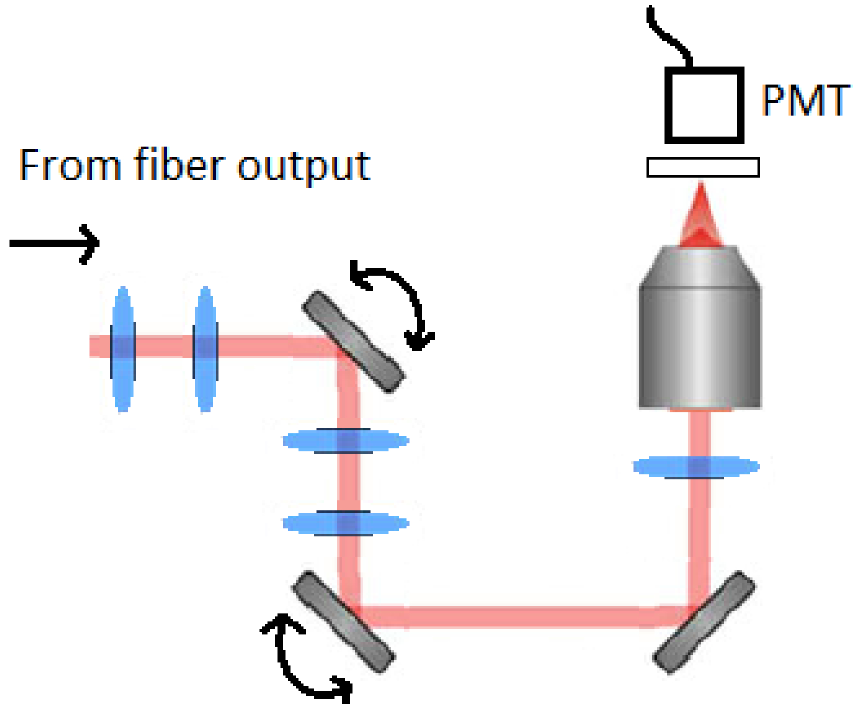

Figure 3.10: Working detail of the SHG microscope scan optics. The objective is 0.75 NA with a working distance of 11 mm, and is not corrected for spherical aberration. The sample is corn starch.

Figure 3.11: Full SHG microscopy of corn starch with BKG filter. Dimensions are 100 μm x 100 μm.

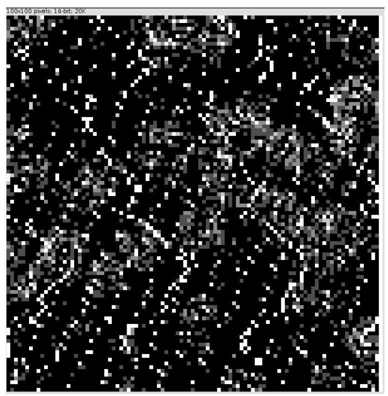

Figure 3.12: Second Harmonic Generation (SHG) microscopy of corn starch with a filter transmitting only 515-525 nm wavelengths. Dimensions are 100 μm x 100 μm.

CHAPTER 4
CONCLUSION

Previous experiments on PCF SC generation have elucidated the delimitations on noise amplification and shot-to-shot stability. By manufacturing a UHNA fiber with the correct specifications, we can avoid the drawbacks of chaotic behavior, while engineering the spectral characteristics for use in MPM. The amount of SPM and diffusion can be tailored by comparing and adjusting the nonlinear and dispersive lengths of the fiber.

The pulse-to-pulse stability of the fiber allows for better use of the continuum for use in nonlinear microscopy, reducing dwell times, for example. By looking at the spectral characterization, we see the spectral spread is toward shorter wavelengths, making it evident that the main mechanisms of broadening are SPM and Stokes broadening. Because the response of the medium is not instantaneous, we have a Stokes-anti-Stokes asymmetry evident in the spectral characterization. By using this light in SHG imaging of corn starch, we can see that the spectral spread from the fiber results in a spectral spread of SHG imaging.

One contributing factor to the low signal-to-noise ratio is the objective used in the SHG microscope. This objective is not corrected for spherical aberration (SA), and thus by imaging the corn starch through a cover slip, SA is added, causing the off axis rays to converge to different focal planes. Because of this added SA, the peak intensity of the beam is lowered, resulting in less MPM advantage, and lower signal-to-noise ratio.

Another reason for low signal-to-noise ratio is the temporal dispersion from the UHNA optical fiber. An estimate of this temporal dispersion is roughly 96.75 ps, which is a lengthening of the pulse by 387 times. A more detailed calculation could be performed in order to better estimate the temporal dispersion in order to correct for it. As shown in Figure 4.1, this temporal dispersion can be corrected by use of a compressing pair of prisms, sending the various wavelength components on paths of different lengths. Compression would increase the peak intensity to reach the sample, increasing the multiphoton advantage, and hence the signal-to-noise ratio.

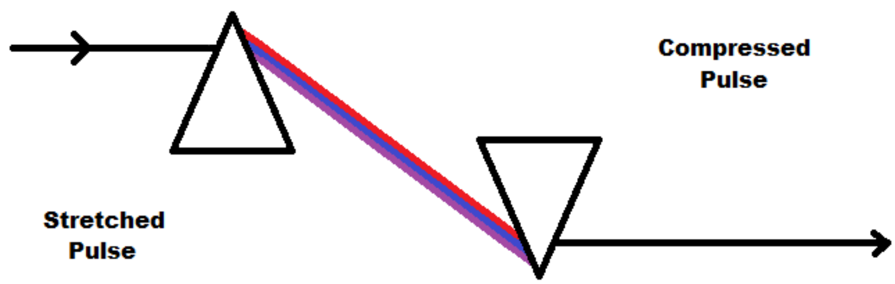

Figure 4.1: Proposed temporal pulse compression to increase peak power and signal-to-noise ratio.

4.1 Extension to multiple foci in microscope

Because of the bandwidth created from UHNA continuum generation, multiple fluorophores are able to be excited with the use of one beam. With use of dMPLSM, each beam from the fiber can be spatially separated, allowing for multiple modalities to be generated with each shot. This can allow for an expansion of parameters to be used, allowing for multiplexing to create large amounts of data in each shot. In addition, by splitting these beams further into different pathways and applying filters, the fluorophoric information can be multiplexed as well. This data can then be electronically demultiplexed, allowing for tracking of multiple fluorophores within a sample simultaneously. In previous experiments simultaneous imaging of up to six planes has been demonstrated [97] [98]. This further expands the differential capabilities of simultaneous imaging.

REFERENCES CITED

[1] Hellwarth, Robert, and Paul Christensen. "Nonlinear optical microscopic examination of structure in polycrystalline ZnSe." *Optics Communications* 12.3 (1974): 318-322.

[2] Sheppard, C. J. R., and R. Kompfner. "Resonant scanning optical microscope." *Applied optics* 17.18 (1978): 2879-2882.

[3] Denk, Winfried, James H. Strickler, and Watt W. Webb. "Two-photon laser scanning fluorescence microscopy." *Science* (New York, NY) 248.4951 (1990): 73.

[4] Davidovits, Paul, and M. D. Egger. "Scanning laser microscope for biological investigations." *Applied Optics* 10.7 (1971): 1615-1619.

[5] GoppertMayer, Maria. "Uber elementarakte mit zwei quantensprungen." *Annalen der Physik* 401.3 (1931): 273-294.

[6] Maiman, Theodore H. "Stimulated optical radiation in ruby." (1960): 493-494.

[7] Kaiser, W., and C. G. B. Garrett. "Two-Photon Excitation in $CaF_2 : Eu^{2+}$." *Physical Review Letters* 7.6 (1961): 229-231.

[8] Singh, S., and L. T. Bradley. "Three-photon absorption in napthalene crystals by laser excitation." *Physical Review Letters* 12.22 (1964): 612-614.

[9] Birge, Robert R. "Two-photon spectroscopy of protein-bound chromophores." *Accounts of Chemical Research* 19.5 (1986): 138-146.

[10] Birge, Robert R., and Brian M. Pierce. "A theoretical analysis of the twophoton properties of linear polyenes and the visual chromophores." *The Journal of Chemical Physics* 70.1 (1979): 165-178.

[11] Birge, Robert R., et al. "Two-photon spectroscopy of all-trans-retinal. Nature of the low-lying singlet states." *Journal of the American Chemical Society* 104.9 (1982): 2519-2525.

[12] Birge, R. R., and L. M. Hubbard. "Molecular dynamics of trans-cis isomerization in bathorhodopsin." *Biophysical journal* 34.3 (1981): 517-534.

[13] Ottolenghi, Michael. "The photochemistry of rhodopsins." *Advances in Photochemistry*, Volume 12 (2007): 97-200.

[14] McClain, W. M. "Excited State Symmetry Assignment Through Polarized Two-Photon Absorption Studies of Fluids." *The Journal of Chemical Physics* 55 (1971): 2789.

[15] Gallant, Daniel J., Brigitte Bouchet, and Paul M. Baldwin. "Microscopy of starch: evidence of a new level of granule organization." *Carbohydrate polymers* 32.3 (1997): 177-191.

[16] Berger, V. "Nonlinear photonic crystals." *Physical Review Letters* 81.19 (1998): 4136-4139.

[17] Pawley, James, ed. *Handbook of biological confocal microscopy.* Springer, 2006.

[18] Jaiswal, Jyoti K., et al. "Long-term multiple color imaging of live cells using quantum dot bioconjugates." *Nature biotechnology* 21.1 (2002): 47-51.

[19] Hoshino, Akiyoshi, et al. "Applications of T-lymphoma labeled with fluorescent quantum dots to cell tracing markers in mouse body." *Biochemical and biophysical research communications* 314.1 (2004): 46-53.

[20] Voura, Evelyn B., et al. "Tracking metastatic tumor cell extravasation with quantum dot nanocrystals and fluorescence emission-scanning microscopy." *Nature medicine* 10.9 (2004): 993-998.

[21] Wokosin, David L., et al. "Threephoton excitation fluorescence imaging of biological specimens using an allsolidstate laser." *Bioimaging* 4.3 (2001): 208-214.

[22] Xu, Chris, and Watt W. Webb. "Measurement of two-photon excitation cross sections of molecular fluorophores with data from 690 to 1050 nm." *JOSA B* 13.3 (1996): 481-491.

[23] Maiti, S., et al. "Measuring serotonin distribution in live cells with three-photon excitation." *Science* 275.5299 (1997): 530-532.

[24] Williams, Rebecca M., et al. "Mucosal mast cell secretion processes imaged using three-photon microscopy of 5-hydroxytryptamine autofluorescence." *Biophysical journal* 76.4 (1999): 1835-1846.

[25] Rehms, Aden A., and Patrik R. Callis. "Two-photon fluorescence excitation spectra of aromatic amino acids." *Chemical physics letters* 208.3 (1993): 276-282.

[26] Svoboda, Karel, and Steven M. Block. "Biological applications of optical forces." *Annual review of biophysics and biomolecular structure* 23.1 (1994): 247-285.

[27] Curley, P. F., et al. "Application of a femtosecond self-sustaining mode-locked Ti: sapphire laser to the field of laser scanning confocal microscopy." *Optical and quantum electronics* 24.8 (1992): 851-859.

[28] Mortensen, O. Sonnich, and E. Nrby Svendsen. "Initial and final molecular states as virtual statesin twophoton processes." *The Journal of Chemical Physics 74.6* (1981): 3185-3189.

[29] Loudon, Rodney. *The quantum theory of light.* Oxford University Press, USA, 2000.

[30] Snyder, Allan W., and J. Love. *Optical waveguide theory.* Vol. 190. Springer, 1983.

[31] Kaiser, P., and H. W. Astle, 1974, Low-loss single material bers made from pure fused silica, *Bell Syst. Tech. J.* 53, 10211039.

[32] Russell, P. St. J., 1991, personal papers, cited in [37].

[33] Knight, J. C., et al. "All-silica single-mode optical fiber with photonic crystal cladding." *Optics Letters* 21.19 (1996): 1547-1549.

[34] Benabid, Fetah, et al. "Stimulated Raman scattering in hydrogen-filled hollow-core photonic crystal fiber." *Science* 298.5592 (2002): 399-402.

[35] Knight, Jonathan C. "Photonic crystal fibres." *Nature* 424.6950 (2003): 847-851.

[36] Ouzounov, Dimitre G., et al. "Generation of megawatt optical solitons in hollow-core photonic band-gap fibers." *Science* 301.5640 (2003): 1702-1704.

[37] Russell, Philip. "Photonic crystal fibers." *Science* 299.5605 (2003): 358-362.

[38] Birks, T. A., J. C. Knight, and P. St J. Russell. "Endlessly single-mode photonic crystal fiber." *Optics Letters* 22.13 (1997): 961-963.

[39] Mogilevtsev, D., T. A. Birks, and P. St J. Russell. "Group-velocity dispersion in photonic crystal fibers." *Optics Letters* 23.21 (1998): 1662-1664.

[40] Broderick, N. G. R., et al. "Nonlinearity in holey optical fibers: measurement and future opportunities." *Optics Letters* 24.20 (1999): 1395-1397.

[41] Ranka, Jinendra K., Robert S. Windeler, and Andrew J. Stentz. "Visible continuum generation in air-silica microstructure optical fibers with anomalous dispersion at 800 nm." *Optics Letters* 25.1 (2000): 25-27.

[42] Wadsworth, W. J., et al. "Soliton effects in photonic crystal fibres at 850 nm." *Electronics Letters* 36.1 (2000): 53-55.

[43] Provino, L., et al. "Compact broadband continuum source based on microchip laser pumped microstructured fibre." *Electronics Letters* 37.9 (2001): 558-560.

[44] Coen, Stephane, et al. "White-light supercontinuum generation with 60-ps pump pulses in a photonic crystal fiber." *Optics Letters* 26.17 (2001): 1356-1358.

[45] Liu, Xiang, et al. "Soliton self-frequency shift in a short tapered airsilica microstructure fiber." *Optics Letters* 26.6 (2001): 358-360.

[46] Washburn, B. R., et al. "Tunable near-infrared femtosecond soliton generation in photonic crystal fibres." *Electronics Letters* 37.25 (2001): 1510-1512.

[47] Husakou, A. V., and J. Herrmann. "Supercontinuum generation of higher-order solitons by fission in photonic crystal fibers." *Physical Review Letters* 87.20 (2001): 203901.

[48] Herrmann, J., et al. "Experimental evidence for supercontinuum generation by fission of higher-order solitons in photonic fibers." *Physical review Letters* 88.17 (2002): 173901.

[49] Udem, Thomas, et al. "A new type of frequency chain and its application to fundamental frequency metrology." *The Hydrogen Atom* (2001): 125-144.

[50] Hollberg, Leo, et al. "Optical frequency standards and measurements." *Quantum Electronics, IEEE Journal of* 37.12 (2001): 1502-1513.

[51] Ivanov, Eugene N., Scott A. Diddams, and Leo Hollberg. "Experimental study of noise properties of a Ti: sapphire femtosecond laser." *Ultrasonics, Ferroelectrics and Frequency Control, IEEE Transactions on* 50.4 (2003): 355-360.

[52] Gu, Xun, et al. "Frequency-resolved optical gating and single-shot spectral measurements reveal fine structure in microstructure-fiber continuum." *Optics Letters* 27.13 (2002): 1174-1176.

[53] Dudley, John M., and Stephane Coen. "Coherence properties of supercontinuum spectra generated in photonic crystal and tapered optical fibers." *Optics Letters* 27.13 (2002): 1180-1182.

[54] Gaeta, Alexander L. "Nonlinear propagation and continuum generation in microstructured optical fibers." *Optics Letters* 27.11 (2002): 924-926.

[55] Theer, Patrick, Mazahir T. Hasan, and Winfried Denk. "Two-photon imaging to a depth of 1000 m in living brains by use of a $Ti : Al_2O_3$ regenerative amplifier." *Optics Letters* 28.12 (2003): 1022-1024.

[56] Brakenhoff, G. J., et al. "Realtime twophoton confocal microscopy using a femtosecond, amplified Ti: sapphire system." *Journal of microscopy* 181.3 (1996): 253-259.

[57] Fork, R. L., O. E. Martinez, and J. P. Gordon. "Negative dispersion using pairs of prisms." *Optics letters* 9.5 (1984): 150-152.

[58] Vidne, Y., and M. Rosenbluh. "Spatial modes in a PCF fiber generated continuum." *Lasers and Electro-Optics, 2006 and 2006 Quantum Electronics and Laser Science Conference.* CLEO/QELS 2006. Conference on. IEEE, 2006.

[59] Steel, M. J., et al. "Symmetry and degeneracy in microstructured optical fibers." *Optics letters* 26.8 (2001): 488-490.

[60] Ortigosa-Blanch, A., et al. "Highly birefringent photonic crystal fibers." *Optics letters* 25.18 (2000): 1325-1327.

[61] Hansen, Theis P., et al. "Highly birefringent index-guiding photonic crystal fibers." *Photonics Technology Letters, IEEE* 13.6 (2001): 588-590.

[62] Lehtonen, M., et al. "Supercontinuum generation in a highly birefringent microstructured fiber." *Applied physics letters* 82.14 (2003): 2197-2199.

[63] Proulx, Antoine, et al. "Intensity and polarization dependences of the supercontinuum generation in birefringent and highly nonlinear microstructured fibers." *Optics express* 11.25 (2003): 3338-3345.

[64] Corwin, K. L., et al. "Fundamental noise limitations to supercontinuum generation in microstructure fiber." *Physical review letters* 90.11 (2003): 113904.

[65] Corwin, K. L., et al. "Fundamental amplitude noise limitations to supercontinuum spectra generated in a microstructured fiber." *Applied Physics B: Lasers and Optics* 77.2 (2003): 269-277.

[66] Ames, J. N., et al. "Excess noise generation during spectral broadening in a microstructured fiber." *Applied Physics B: Lasers and Optics* 77.2 (2003): 279-284.

[67] Haverkamp, Nils, and Harald Telle. "Complex intensity modulation transfer function for supercontinuum generation in microstructure fibers." *Optics Express* 12.4 (2004): 582-587.

[68] Gu, Xun, et al. "Experimental studies of the coherence of microstructure-fiber supercontinuum." *Optical Express* 11.21 (2003): 2697-2703.

[69] Lu, Fei, and Wayne H. Knox. "Generation of a broadband continuum with high spectral coherence in tapered single-mode optical fibers." *Conference on Lasers and Electro-Optics.* Optical Society of America, 2004.

[70] Kobtsev, S. M., et al. "Coherent, polarization and temporal properties of self-frequency shifted solitons generated in polarization-maintaining microstructured fibre." *Applied Physics B: Lasers and Optics* 81.2 (2005): 265-269.

[71] Zeylikovich, Iosif, Vladimir Kartazaev, and R. R. Alfano. "Spectral, temporal, and coherence properties of supercontinuum generation in microstructure fiber." *JOSA B* 22.7 (2005): 1453-1460.

[72] Lak, S., et al. "Pulse compression of nanojoule pulses in the visible using microstructure optical fiber and dispersion compensation." *Applied Physics B: Lasers and Optics* 76.3 (2003): 267-275.

[73] Druon, Frdric, and Patrick Georges. "Pulse compression down to 20 fs using a photonic crystal fiber seeded by a diode-pumped Yb: SYS laser at 1070 nm." *Optics express* 12.15 (2004): 3383-3396.

[74] McConnell, Gail, and Erling Riis. "Ultra-short pulse compression using photonic crystal fibre." *Applied Physics B: Lasers and Optics* 78.5 (2004): 557-563.

[75] Dudley, John, and Stphane Coen. "Fundamental limits to few-cycle pulse generation from compression of supercontinuum spectra generated in photonic crystal fiber." *Optics Express* 12.11 (2004): 2423-2428.

[76] Chang, Guoqing, Theodore B. Norris, and Herbert G. Winful. "Optimization of supercontinuum generation in photonic crystal fibers for pulse compression." *Optics letters* 28.7 (2003): 546-548.

[77] Schenkel, Birgit, Rdiger Paschotta, and Ursula Keller. "Pulse compression with supercontinuum generation in microstructure fibers." *JOSA B* 22.3 (2005): 687-693.

[78] Adachi, Muneyuki, et al. "Sub-5-fs pulse compression of laser output using photonic crystal fiber with short zero-dispersion wavelength." *Japanese journal of applied physics* 44 (2005): L1423-L1425.

[79] Hartl, I., et al. "Ultrahigh-resolution optical coherence tomography using continuum generation in an airsilica microstructure optical fiber." *Optics Letters* 26.9 (2001): 608-610.

[80] Wang, Yimin, et al. "Ultrahigh-resolution optical coherence tomography by broadband continuum generation from a photonic crystal fiber." *Optics letters* 28.3 (2003): 182-184.

[81] Povazay, Boris, et al. "Submicrometer axial resolution optical coherence tomography." *Optics Letters* 27.20 (2002): 1800-1802.

[82] Bourquin, S., et al. "Ultrahigh resolution real time OCT imaging using a compact femtosecond Nd: Glass laser and nonlinear fiber." *Optics express* 11.24 (2003): 3290-3297.

[83] Humbert, Georges, et al. "Supercontinuum generation system for optical coherence tomography based on tapered photonic crystal fibre." *Optics express* 14.4 (2006): 1596-1603.

[84] Andresen, Esben Ravn, et al. "Broadband multiplex coherent anti-Stokes Raman scattering microscopy employing photonic-crystal fibers." *JOSA B* 22.9 (2005): 1934-1938.

[85] Wang, Haifeng, Terry B. Huff, and Ji-Xin Cheng. "Coherent anti-Stokes Raman scattering imaging with a laser source delivered by a photonic crystal fiber." *Optics letters* 31.10 (2006): 1417-1419.

[86] Andresen, Esben R., et al. "Fiber laser-based light source for coherent anti-Stokes Raman scattering microspectroscopy." *Optics express* 15.8 (2007): 4848-4856.

[87] Okuno, Masanari, et al. "Ultrabroadband multiplex CARS microspectroscopy and imaging using a subnanosecond supercontinuum light source in the deep near infrared." *Optics letters* 33.9 (2008): 923-925.

[88] McConnell, Gail. "Confocal laser scanning fluorescence microscopy with a visible continuum source." *Optics Express* 12.13 (2004): 2844-2850.

[89] Fu, Ling, and Min Gu. "Double-clad photonic crystal fiber coupler for compact nonlinear optical microscopy imaging." *Optics letters* 31.10 (2006): 1471-1473.

[90] Isobe, Keisuke, et al. "Multi-spectral two-photon excited fluorescence microscopy using supercontinuum light source." *Japanese journal of applied physics* 44 (2005): L167-L169.

[91] Palero, J. A., et al. "Short-wavelength two-photon excitation fluorescence microscopy of tryptophan with a photonic crystal fiber based light source." *Opt. Express* 13.14 (2005): 5363-5368.

[92] Unruh, Jay R., et al. "Two-photon microscopy with wavelength switchable fiber laser excitation." *Opt. Express* 14.21 (2006): 9825-9831.

[93] Field, Jeffrey J., et al. "Differential multiphoton laser scanning microscopy." Selected Topics in *Quantum Electronics, IEEE Journal of* 18.1 (2012): 14-28.

[94] Cremer, Christoph, and Thomas Cremer. "Considerations on a laser-scanning-microscope with high resolution and depth of field." *Microscopica acta* (1974): 31-44.

[95] Bewersdorf, Jrg, Rainer Pick, and Stefan W. Hell. "Multifocal multiphoton microscopy." *Optics letters* 23.9 (1998): 655-657.

[96] Helmchen, Fritjof, and Winfried Denk. "New developments in multiphoton microscopy." *Current opinion in neurobiology* 12.5 (2002): 593-601.

[97] Sheetz, Kraig E., et al. "Advancing multifocal nonlinear microscopy: development and application of a novel multibeam $Yb : KGd(WO_4)_2$ oscillator." *Optics express* 16.22 (2008): 17574-17584.

[98] Cheng, Adrian, et al. "Simultaneous two-photon calcium imaging at different depths with spatiotemporal multiplexing." *Nature methods* 8.2 (2011): 139-142.

[99] Nakazawa, Masataka, et al. "Coherence degradation in the process of supercontinuum generation in an optical fiber." *Optical Fiber Technology* 4.2 (1998): 215-223.

[100] Kubota, Hirokazu, Kohichi R. Tamura, and Masataka Nakazawa. "Analyses of coherence-maintained ultrashort optical pulse trains and supercontinuum generation in the presence of solitonamplified spontaneous-emission interaction." *JOSA B* 16.12 (1999): 2223-2232.

[101] Nowak, George A., Jaeyoun Kim, and Mohammed N. Islam. "Stable supercontinuum generation in short lengths of conventional dispersion-shifted fiber." *Applied Optics* 38.36 (1999): 7364-7369.

[102] Agrawal, Govind P. *Applications of nonlinear fiber optics.* Vol. 10. Academic press, 2008.

[103] Bloembergen, N., and P. Lallemand. "Complex intensity-dependent index of refraction, frequency broadening of stimulated Raman lines, and stimulated Rayleigh scattering." *Physical Review Letters* 16.3 (1966): 81-84.

[104] Brewer, Richard G. "Frequency shifts in self-focused light." *Physical Review Letters* 19.1 (1967): 8-10.

[105] Cheung, A. C., et al. "Phase modulation of Q-switched laser beams in small-scale filaments." *Physical Review Letters* 20.15 (1968): 786-789.

[106] Lallemand, P. "Temperature variation of the width of stimulated Raman lines in liquids." *Applied Physics Letters* 8.11 (1966): 276-277.

[107] Jones, W. J., and B. P. Stoicheff. "Inverse Raman spectra: induced absorption at optical frequencies." *Physical Review Letters* 13.22 (1964): 657-659.

[108] Shimizu, Fujio. "Frequency broadening in liquids by a short light pulse." *Physical Review Letters* 19.19 (1967): 1097-1100.

[109] Stoicheff, B.P. "Characteristics of stimulated Raman radiation generated by coherent light." *Physics Letters* 7 (1963): 186.

[110] Marburger, J.H. "Self-focusing: theory." *Prog. Quantum Electron.* 4 (1975): 35.

[111] Shen Y.R. "Self-focusing: experimental." *Prog. Quantum Electron.* 4 (1975) 1.

[112] Gustafson, T. K., et al. "Self-modulation, self-steepening, and spectral development of light in small-scale trapped filaments." *Physical Review* 177.1 (1969): 306.

[113] Manassah, Jamal T., Robert R. Alfano, and Mustafa Mustafa. "Spectral distribution of an ultrafast supercontinuum laser source." *Physics Letters A* 107.7 (1985): 305-309.

[114] Manassah, J., et al. "Spectral extent and pulse shape of the supercontinuum for ultrashort laser pulse." *Quantum Electronics, IEEE Journal of* 22.1 (1986): 197-204.

[115] Yang, Guozhen, and Y. R. Shen. "Spectral broadening of ultrashort pulses in a nonlinear medium." *Optics letters* 9.11 (1984): 510-512.

[116] Shen, Yuen-Ron. *The principles of nonlinear optics.* New York, Wiley-Interscience, 1984, 575 p. 1 (1984).

[117] Fork, Richard L., et al. "Compression of optical pulses to six femtoseconds by using cubic phase compensation." *Optics Letters* 12.7 (1987): 483-485.

[118] Mitschke, Fedor M., and Linn F. Mollenauer. "Discovery of the soliton self-frequency shift." *Optics Letters* 11.10 (1986): 659-661.

[119] Gordon, James P. "Theory of the soliton self-frequency shift." *Optics letters* 11.10 (1986): 662-664.

[120] Kodama, Yuji, and Akira Hasegawa. "Nonlinear pulse propagation in a monomode dielectric guide." *Quantum Electronics, IEEE Journal of* 23.5 (1987): 510-524.

[121] Smith, R. G. "Optical power handling capacity of low loss optical fibers as determined by stimulated Raman and Brillouin scattering." *Applied Optics* 11.11 (1972): 2489-2494.

[122] Marcuse, Dietrich. "Pulse distortion in single-mode fibers. 3: Chirped pulses." *Applied Optics* 20.20 (1981): 3573-3579.

[123] Mollenauer, Linn F., Roger H. Stolen, and James P. Gordon. "Experimental observation of picosecond pulse narrowing and solitons in optical fibers." *Physical Review Letters* 45.13 (1980): 1095-1098.

[124] Grischkowsky, D., and A. C. Balant. "Optical pulse compression based on enhanced frequency chirping." *Applied Physics Letters* 41.1 (1982): 1-3.

[125] Tomlinson, W. J., R. H. Stolen, and C. V. Shank. "Compression of optical pulses chirped by self-phase modulation in fibers." *JOSA B* 1.2 (1984): 139-149.

[126] Zakharov, Vo E., and AB V. Shabat. "Exact theory of two-dimensional self-focusing and one-dimensional self-modulation of waves in nonlinear media(Differential equation solution for plane self focusing and one dimensional self modulation of waves interacting in nonlinear media)." *Soviet Physics-JETP* 34 (1972): 62-69.

[127] Hasegawa, Akira, and Frederick Tappert. "Transmission of stationary nonlinear optical pulses in dispersive dielectric fibers. I. Anomalous dispersion." *Applied Physics Letters* 23.3 (1973): 142-144.

[128] Fleck, J. A., J. R. Morris, and M. D. Feit. "Time-dependent propagation of high energy laser beams through the atmosphere." *Applied Physics A: Materials Science Processing* 10.2 (1976): 129-160.

[129] Lax, M., J. H. Batteh, and G. P. Agrawal. "Channeling of intense electromagnetic beams." *Journal of Applied Physics* 52.1 (1981): 109-125.

[130] Agrawal, Govind P., and M. J. Potasek. "Nonlinear pulse distortion in single-mode optical fibers at the zero-dispersion wavelength." *Physical Review A* 33.3 (1986): 1765.

[131] Tomlinson, W. J., Roger H. Stolen, and Anthony M. Johnson. "Optical wave breaking of pulses in nonlinear optical fibers." *Optics letters* 10.9 (1985): 457-459.

[132] Alfano, Robert R. "The supercontinuum laser source." (1989).